INTERDISCIPLINARY APPLIED MATHEMATICS

MATHEMATICAL BIOLOGY

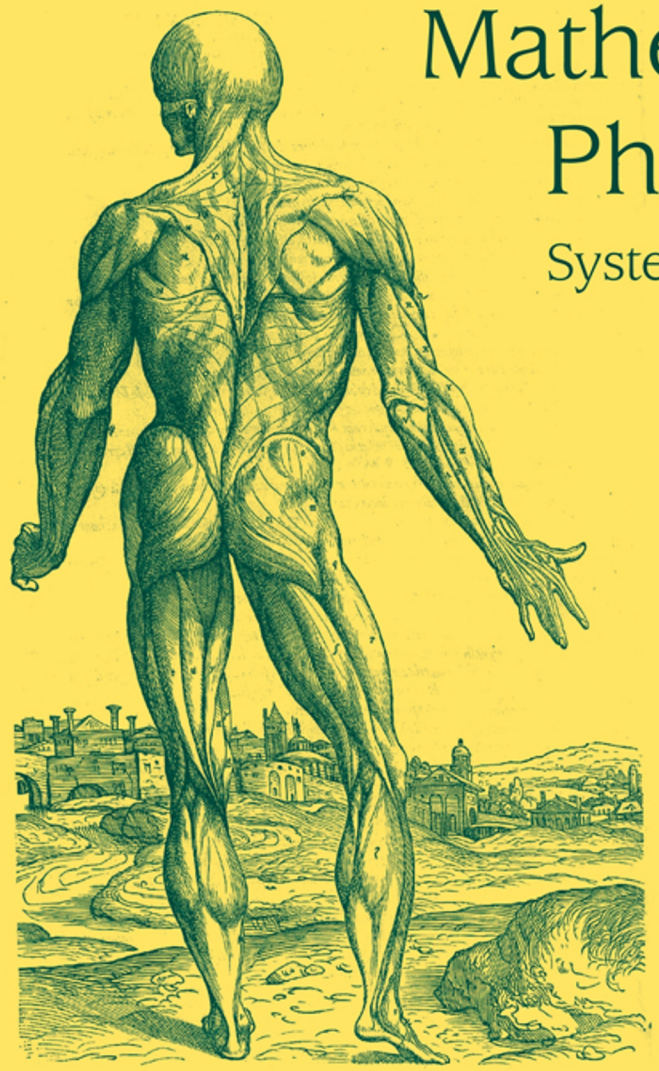

Mathematical Physiology

Systems Physiology

James Keener
James Sneyd

Second Edition

Springer

Interdisciplinary Applied Mathematics

Volume 8/I

Problems in engineering, computational science, and the physical and biological sciences are using increasingly sophisticated mathematical techniques. Thus, the bridge between the mathematical sciences and other disciplines is heavily traveled. The correspondingly increased dialog between the disciplines has led to the establishment of the series: *Interdisciplinary Applied Mathematics*.

The purpose of this series is to meet the current and future needs for the interaction between various science and technology areas on the one hand and mathematics on the other. This is done, firstly, by encouraging the ways that mathematics may be applied in traditional areas, as well as point towards new and innovative areas of applications; and, secondly, by encouraging other scientific disciplines to engage in a dialog with mathematicians outlining their problems to both access new methods and suggest innovative developments within mathematics itself.

The series will consist of monographs and high-level texts from researchers working on the interplay between mathematics and other fields of science and technology.

CHAPTER 5

Excitability

We have seen in previous chapters that the control of cell volume results in a potential difference across the cell membrane, and that this potential difference causes ionic currents to flow through channels in the cell membrane. Regulation of this membrane potential by control of the ionic channels is one of the most important cellular functions. Many cells, such as neurons and muscle cells, use the membrane potential as a signal, and thus the operation of the nervous system and muscle contraction (to name but two examples) are both dependent on the generation and propagation of electrical signals.

To understand electrical signaling in cells, it is helpful (and not too inaccurate) to divide all cells into two groups: excitable cells and nonexcitable cells. Many cells maintain a stable equilibrium potential. For some, if currents are applied to the cell for a short period of time, the potential returns directly to its equilibrium value after the applied current is removed. Such cells are nonexcitable, typical examples of which are the epithelial cells that line the walls of the gut. Photoreceptors (Chapter 19) are also nonexcitable, although in their case, membrane potential plays an extremely important signaling role nonetheless.

However, there are cells for which, if the applied current is sufficiently strong, the membrane potential goes through a large excursion, called an *action potential*, before eventually returning to rest. Such cells are called *excitable*. Excitable cells include cardiac cells, smooth and skeletal muscle cells, some secretory cells, and most neurons. The most obvious advantage of excitability is that an excitable cell either responds in full to a stimulus or not at all, and thus a stimulus of sufficient amplitude may be reliably distinguished from background noise. In this way, noise is filtered out, and a signal is reliably transmitted.

There are many examples of excitability that occur in nature. A simple example of an excitable system is a household match. The chemical components of the match head are stable to small fluctuations in temperature, but a sufficiently large temperature fluctuation, caused, for example, by friction between the head and a rough surface, triggers the abrupt oxidation of these chemicals with a dramatic release of heat and light. The fuse of a stick of dynamite is a one-dimensional continuous version of an excitable medium, and a field of dry grass is its two-dimensional version. Both of these spatially extended systems admit the possibility of wave propagation (Chapter 6). The field of grass has one additional feature that the match and dynamite fuse fail to have, and that is recovery. While it is not very rapid by physiological standards, given a few months of growth, a burned-over field of grass will regrow enough fuel so that another fire may spread across it.

Although the generation and propagation of signals have been extensively studied by physiologists for at least the past 100 years, the most important landmark in these studies is the work of Alan Hodgkin and Andrew Huxley, who developed the first quantitative model of the propagation of an electrical signal along a squid giant axon (deemed "giant" because of the size of the axon, *not* the size of the squid). Their model was originally used to explain the action potential in the long giant axon of a squid nerve cell, but the ideas have since been extended and applied to a wide variety of excitable cells. Hodgkin–Huxley theory is remarkable, not only for its influence on electrophysiology, but also for its influence, after some filtering, on applied mathematics. FitzHugh (in particular) showed how the essentials of the excitable process could be distilled into a simpler model on which mathematical analysis could make some progress. Because this simplified model turned out to be of such great theoretical interest, it contributed enormously to the formation of a new field of applied mathematics, the study of excitable systems, a field that continues to stimulate a vast amount of research.

Because of the central importance of cellular electrical activity in physiology, because of the importance of the Hodgkin–Huxley equations in the study of electrical activity, and because it forms the basis for the study of excitability, it is no exaggeration to say that the Hodgkin–Huxley equations are the most important model in all of the physiological literature.

5.1 The Hodgkin–Huxley Model

In Chapter 2 we described how the cell membrane can be modeled as a capacitor in parallel with an ionic current, resulting in the equation

$$C_m \frac{dV}{dt} + I_{\text{ion}}(V,t) = 0, \tag{5.1}$$

where V, as usual, denotes the internal minus the external potential ($V = V_i - V_e$). In the squid giant axon, as in many neural cells, the principal ionic currents are the

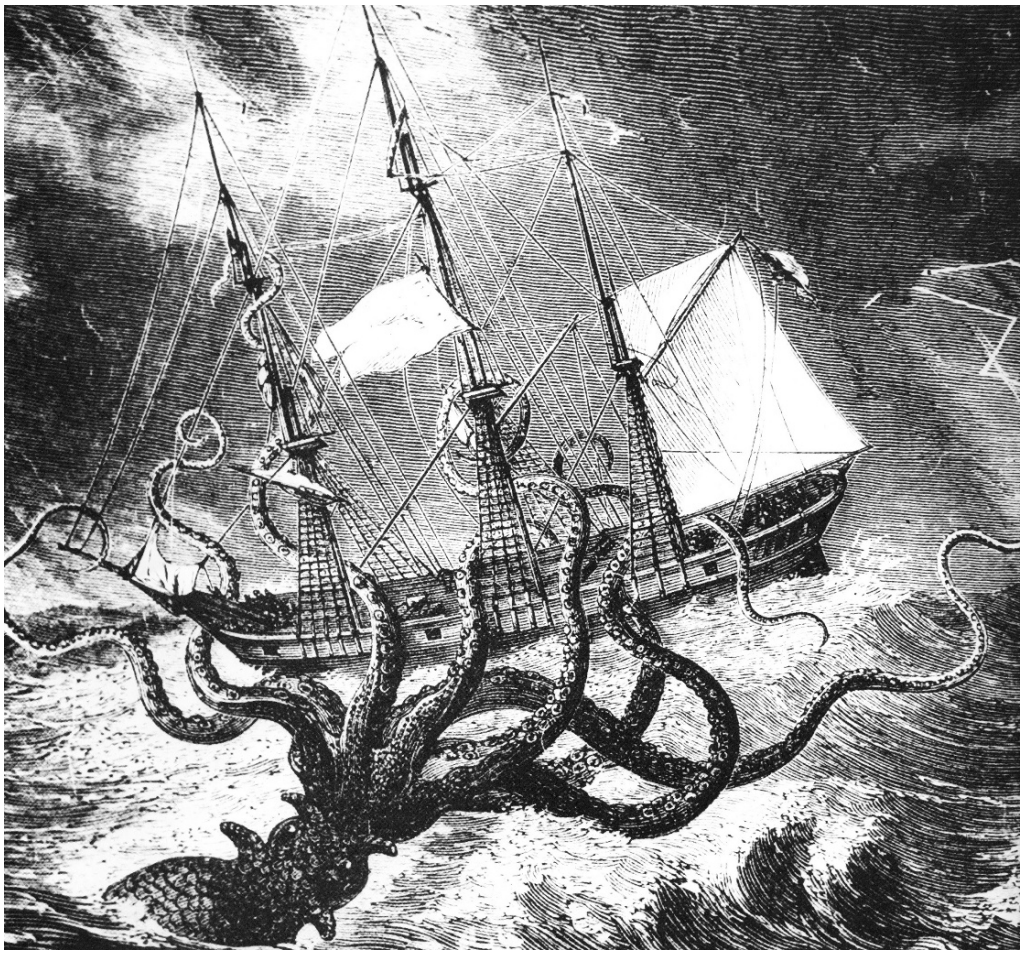

Figure 5.1 The infamous giant squid (or even octopus, if you wish to be pedantic), having nothing to do with the work of Hodgkin and Huxley on squid giant axon. From *Dangerous Sea Creatures*, © 1976, 1977 Time-Life Films, Inc.

Na^+ current and the K^+ current. Although there are other ionic currents, primarily the Cl^- current, in the Hodgkin–Huxley theory they are small and lumped together into one current called the *leakage current*. Since the instantaneous I–V curves of open Na^+ and K^+ channels in the squid giant axon are approximately linear, (5.1) becomes

$$C_m \frac{dV}{dt} = -g_{\mathrm{Na}}(V - V_{\mathrm{Na}}) - g_{\mathrm{K}}(V - V_{\mathrm{K}}) - g_{\mathrm{L}}(V - V_{\mathrm{L}}) + I_{\mathrm{app}}, \tag{5.2}$$

where I_{app} is the applied current. During an action potential there is a measured influx of 3.7 pmoles/cm^2 of Na^+ and a subsequent efflux of 4.3 pmoles/cm^2 of K^+. These

amounts are so small that it is realistic to assume that the ionic concentrations, and hence the equilibrium potentials, are constant and unaffected by an action potential. It is important to emphasize that the choice of linear I–V curves for the three different channel types is dictated largely by experimental data. Axons in other species (such as vertebrates) have ionic channels that are better described by other I–V curves, such as the GHK current equation (2.123). However, the qualitative nature of the results remains largely unaffected, and so the discussion in this chapter, which is mostly of a qualitative nature, remains correct for models that use more complex I–V curves to describe the ionic currents.

Equation (5.2) is a first-order ordinary differential equation and can be written in the form

$$C_m \frac{dV}{dt} = -g_{\text{eff}}(V - V_{\text{eq}}) + I_{\text{app}}, \tag{5.3}$$

where $g_{\text{eff}} = g_{\text{Na}} + g_{\text{K}} + g_{\text{L}}$ and $V_{\text{eq}} = (g_{\text{Na}}V_{\text{Na}} + g_{\text{K}}V_{\text{K}} + g_{\text{L}}V_{\text{L}})/g_{\text{eff}}$. V_{eq} is the membrane resting potential and is a balance between the reversal potentials for the three ionic currents. In fact, at rest, the Na^+ and leakage conductances are small compared to the K^+ conductance, so that the resting potential is close to the K^+ equilibrium potential.

The quantity $R_m = 1/g_{\text{eff}}$, the passive membrane resistance, is on the order of 1000 $\Omega\,\text{cm}^2$. The time constant for this equation is

$$\tau_m = C_m R_m, \tag{5.4}$$

on the order of 1 msec. It follows that, with a steady applied current, the membrane potential should equilibrate quickly to

$$V = V_{\text{eq}} + R_m I_{\text{app}}. \tag{5.5}$$

For sufficiently small applied currents this is indeed what happens. However, for larger applied currents the response is quite different. Assuming that the model (5.2) is correct, the only possible explanation for these differences is that the conductances are not constant but depend in some way on the voltage. Historically, the key step to determining the conductances was being able to measure the individual ionic currents and from this to deduce the changes in conductances. This was brilliantly accomplished by Hodgkin and Huxley in 1952.

5.1.1 History of the Hodgkin–Huxley Equations

(This section is adapted from Rinzel, 1990.) In a series of five articles that appeared in the *Journal of Physiology* in 1952, Alan Lloyd Hodgkin and Andrew Fielding Huxley, along with Bernard Katz, who was a coauthor of the lead paper and a collaborator in several related studies, unraveled the dynamic ionic conductances that generate the nerve action potential (Hodgkin et al., 1952; Hodgkin and Huxley, 1952a,b,c,d). They were awarded the 1963 Nobel Prize in Physiology or Medicine (shared with John C. Eccles, for his work on potentials and conductances at motorneuron synapses).

Before about 1939, the membrane potential was believed to play an important role in the membrane's state, but there was no way to measure it. It was known that a cell's membrane separated different ionic concentrations inside and outside the cell. Applying the Nernst equation, Bernstein (1902) was led to suggest that the resting membrane was semipermeable to K^+, implying that, at rest, V should be around -70 mV. He believed that during activity there was a breakdown in the membrane's resistance to all ionic fluxes, and potential differences would disappear, i.e., V would approach zero.

In 1940, Cole and Curtis, using careful electrode placement coupled with biophysical and mathematical analysis, obtained the first convincing evidence for a substantial transient increase in membrane conductivity during passage of the action potential. While they estimated a large conductance increase, it was not infinite, so without a direct measurement of membrane potential it was not possible to confirm or nullify Bernstein's hypothesis. During a postdoctoral year in the U.S. in 1937–1938, Hodgkin established connections with Cole's group at Columbia and worked with them at Woods Hole in the summer. He and Curtis nearly succeeded in measuring V directly by tunneling along the giant axon with a glass micropipette. When each succeeded later (separately, with other collaborators), they found, surprisingly, that V rose transiently toward zero, but with a substantial overshoot. This finding brought into serious question the hypothesis of Bernstein and provided much food for thought during World War II, when Hodgkin, Huxley, and many other scientists were involved in the war effort.

By the time postwar experimental work was resuming in England, Cole and Marmont had developed the *space-clamp technique*. This method allowed one to measure directly the total transmembrane current, uniform through a known area, rather than spatially nonuniform as generated by a capillary electrode. To achieve current control with space clamping, the axon was threaded with a metallic conductor (like a thin silver wire) to provide low axial resistance and thereby eliminate voltage gradients along the length of the axon. Under these conditions the membrane potential is no longer a function of distance along the axon, only of time. In addition, during the 1947 squid season, Cole and company made substantial progress toward controlling the membrane potential as well.

In 1948, Hodgkin went to visit Cole (then at Chicago) to learn directly of their methods. With some further developments of their own, Hodgkin, Huxley, and Katz applied the techniques with great success to record transient ionic fluxes over the physiological ranges of voltages. Working diligently, they collected most of the data for their papers in the summer of 1949. Next came the step of identifying the individual contributions of the different ion species. Explicit evidence that both Na^+ and K^+ were important came from the work of Hodgkin and Katz (1949). This also explained the earlier puzzling observations that V overshoots zero during an action potential, opposing the suggestion of Bernstein. Instead of supposing that there was a transient increase in permeability identical for all ions, Hodgkin and Katz realized that different changes in permeabilities for different ions could account for the V time course, as V would approach the Nernst potential for the ion to which the membrane was predominantly permeable, and

this dominance could change with time. For example, at rest the membrane is most permeable to K^+, so that V is close to V_K. However, if g_K were to decrease and g_{Na} were to increase, then V would be pushed toward V_{Na}, which is positive, thus depolarizing the cell.

The question of how the changes in permeability were dynamically linked to V was not completely stated until the papers of 1952. In fact, the substantial delay from data collection in 1949 until final publication in 1952 can be attributed to the considerable time devoted to data analysis, model formulation, and testing. Computer downtime was also a factor, as some of the solutions of the Hodgkin–Huxley equations were computed on a desktop, hand-cranked calculator. As Hodgkin notes, "The propagated action potential took about three weeks to complete and must have been an enormous labour for Andrew [Huxley]" (Hodgkin, 1976, p. 19).

The final paper of the 1952 series is a masterpiece of the scientific art. Therein they present their elegant experimental data, a comprehensive theoretical hypothesis, a fit of the model to the experimental data (obtained for fixed values of the membrane potential), and then, presto, a prediction (from their numerical computations) of the time course of the propagated action potential. In biology, where quantitatively predictive theories are rare, this work stands out as one of the most successful combinations of experiment and theory.

5.1.2 Voltage and Time Dependence of Conductances

The key step to sorting out the dynamics of the conductances came from the development of the *voltage clamp*. A voltage clamp fixes the membrane potential, usually by a rapid step from one voltage to another, and then measures the current that must be supplied in order to hold the voltage constant. Since the supplied current must equal the transmembrane current, the voltage clamp provides a way to measure the transient transmembrane current that results. The crucial point is that the voltage can be stepped from one constant level to another, and so the ionic currents can be measured at a constant, known, voltage. Thus, even when the conductances are functions of the voltage (as is actually the case), a voltage clamp eliminates any voltage changes and permits measurement of the conductances as functions of time only.

Hodgkin and Huxley found that when the voltage was stepped up and held fixed at a higher level, the total ionic current was initially inward, but at later times an outward current developed (Fig. 5.2). For a number of reasons, not discussed here, they argued that the initial inward current is carried almost entirely by Na^+, while the outward current that develops later is carried largely by K^+. With these assumptions, Hodgkin and Huxley were able to use a clever trick to separate the total ionic current into its constituent ionic parts. They replaced 90% of the extracellular Na^+ in the normal seawater bath with choline (a viscous liquid vitamin B complex found in many animal and vegetable tissues), which rendered the axon nonexcitable but changed the resting potential only slightly. Since it is assumed that immediately after the voltage has been stepped up, the ionic current is all carried by Na^+, it is possible to measure

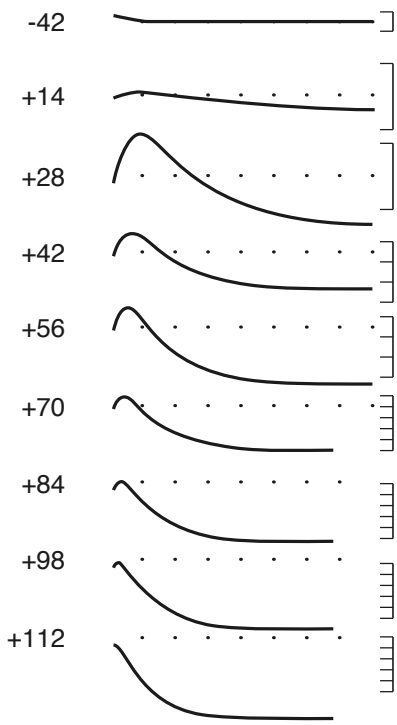

Figure 5.2 Experimental results describing the total membrane current in response to a step depolarization. The numbers on the left give the final value of the membrane potential, in mV. The interval between dots on the horizontal scale is 1 ms, while one division on the vertical scale represents 0.5 mA/cm^2. (Hodgkin and Huxley, 1952a, Fig. 2a.)

the initial Na^+ currents in response to a voltage step. Note that although the Na^+ currents can be measured directly immediately after the voltage step, they cannot be measured directly over a longer time period, as the total ionic current begins to include a contribution from the K^+ current. If we denote the Na^+ currents for the two cases of normal extracellular Na^+ and zero extracellular Na^+ by I^1_{Na} and I^2_{Na} respectively, then the ratio of the two currents,

$$I^1_{Na}/I^2_{Na} = K, \tag{5.6}$$

say, can be measured directly from the experimental data.

Next, Hodgkin and Huxley made two further assumptions. First, they assumed that the Na^+ current ratio K is independent of time and is thus constant over the course of each voltage clamp experiment. In other words, the amplitude and direction of the Na^+ current may be affected by the low extracellular Na^+ solution, but its time course is not. Second, they assumed that the K^+ channels are unaffected by the change in extracellular Na^+ concentration. There is considerable evidence that the Na^+ and K^+ channels are independent. Tetrodotoxin (TTX) is known to block Na^+ currents while leaving the K^+ currents almost unaffected, while tetraethylammonium (TEA) has the opposite effect of blocking the K^+ current but not the Na^+ current. To complete the argument, since $I_{ion} = I_{Na} + I_K$, and $I^1_K = I^2_K$, it follows that $I^1_{ion} - I^1_{Na} = I^2_{ion} - I^2_{Na}$, and

thus

$$I^1_{\mathrm{Na}} = \frac{K}{K-1}(I^1_{\mathrm{ion}} - I^2_{\mathrm{ion}}), \tag{5.7}$$

$$I_{\mathrm{K}} = \frac{I^1_{\mathrm{ion}} - KI^2_{\mathrm{ion}}}{1-K}. \tag{5.8}$$

Hence, given measurements of the total ionic currents in the two cases, and given the ratio K of the Na^+ currents, it is possible to determine the complete time courses of both the Na^+ and K^+ currents.

Finally, from knowledge of the individual currents, one obtains the conductances as

$$g_{\mathrm{Na}} = \frac{I_{\mathrm{Na}}}{V - V_{\mathrm{Na}}}, \qquad g_{\mathrm{K}} = \frac{I_{\mathrm{K}}}{V - V_{\mathrm{K}}}. \tag{5.9}$$

Note that this result relies on the specific (linear) model used to describe the I–V curve of the Na^+ and K^+ channels, but, as stated above, we assume throughout that the instantaneous I–V curves of the Na^+ and K^+ channels are linear.

Samples of Hodgkin and Huxley's data are shown in Fig. 5.3. The plots show ionic conductances as functions of time following a step increase or decrease in the membrane potential. The important observation is that with voltages fixed, the conductances are time-dependent. For example, when V is stepped up and held fixed at a higher level, g_{K} does not increase instantaneously, but instead increases over time to a final steady level. Both the time constant of the increase and the final value of g_{K} are dependent on the value to which the voltage is stepped. Further, g_{K} increases in a sigmoidal fashion, with a slope that first increases and then decreases (Fig. 5.3A and B). Following a step decrease in the voltage, g_{K} falls in a simple exponential fashion (Fig. 5.3A). This particular feature of g_{K}—a sigmoidal increase coupled with an exponential decrease—is important in what follows when we model g_{K}. The behavior of g_{Na} is more complex. Following a step increase in voltage, g_{Na} first increases, but then decreases again, *all at the same fixed voltage* (Fig. 5.3C). Hence, the time dependence of g_{Na} requires a more complex model than for that of g_{K}.

The Potassium Conductance

From the experimental data shown in Fig. 5.3A and B, it is reasonable to expect that g_{K} obeys some differential equation,

$$\frac{dg_{\mathrm{K}}}{dt} = f(v,t), \tag{5.10}$$

say, where $v = V - V_{\mathrm{eq}}$; i.e., v is the difference between the membrane potential and the resting potential. (Of course, since V_{eq} is a constant, $dv/dt = dV/dt$.) However, for g_{K} to have the required sigmoidal increase and exponential decrease, Hodgkin and Huxley realized that it would be easier to write g_{K} as some power of a different variable, n say,

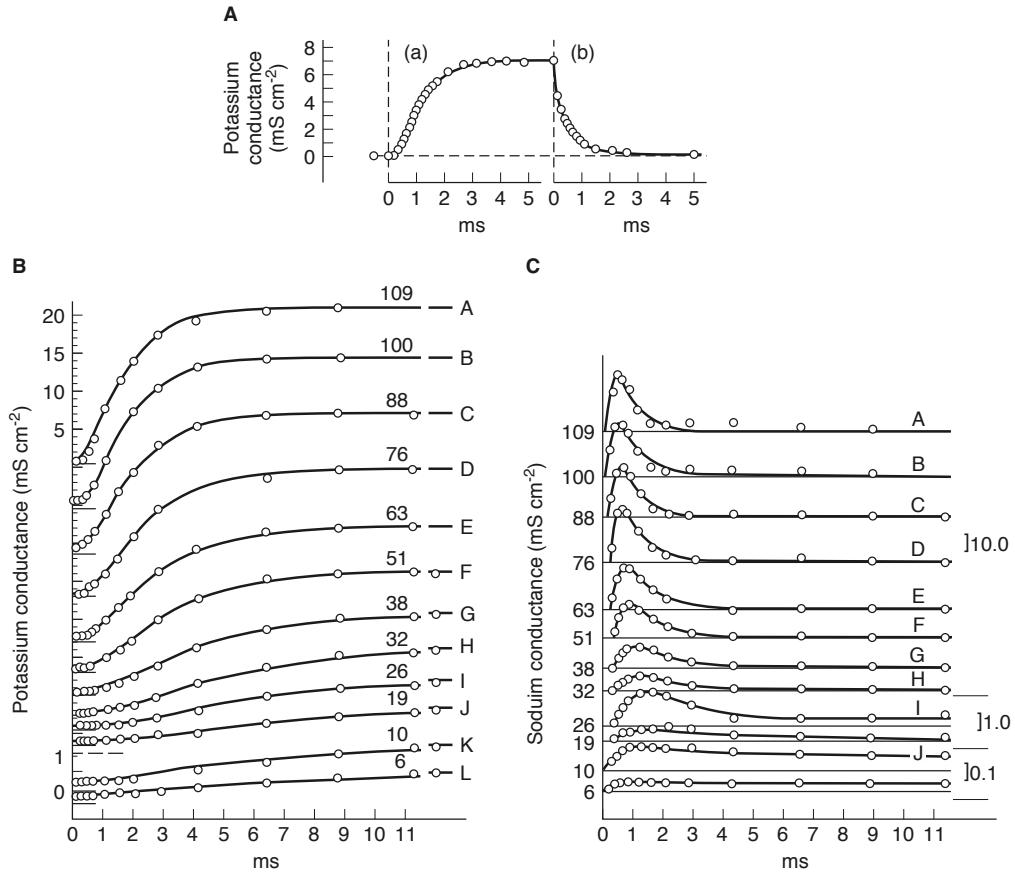

Figure 5.3 Conductance changes as a function of time at different voltage clamps. A: The response of g_K to a step increase in V and then a step decrease. B: Responses of g_K to step increases in V of varying magnitudes. The number on each curve gives the depolarization in mV, and the smooth curves are calculated from solution of (5.11) and (5.12), with the initial condition $g_K(t = 0) = 0.24$ mS/cm^2. The vertical scale is the same in curves A–J, but is increased by a factor of four in the lower two curves. For clarity, the baseline of each curve has been shifted up. C: Responses of g_{Na} to step increases in V of magnitudes given by the numbers on the left, in mV. The smooth curves are the model solutions. The vertical scales on the right are in units of mS/cm^2. (Hodgkin and Huxley, 1952d, Figs. 2, 3, and 6.)

where n satisfies a first-order differential equation. Thus, they wrote

$$g_K = \bar{g}_K n^4, \tag{5.11}$$

for some constant $\bar{g}_K$. The fourth power was chosen not for physiological reasons, but because it was the smallest exponent that gave acceptable agreement with the experimental data. The secondary variable n obeys the differential equation

$$\tau_n(v)\frac{dn}{dt} = n_\infty(v) - n, \tag{5.12}$$

for some functions $\tau_n(v)$ and $n_\infty(v)$ that must be determined from the experimental data in a manner that is described below. Equation (5.12) is often written in the form

$$\frac{dn}{dt} = \alpha_n(v)(1-n) - \beta_n(v)n, \tag{5.13}$$

where

$$n_\infty(v) = \frac{\alpha_n(v)}{\alpha_n(v) + \beta_n(v)}, \tag{5.14}$$

$$\tau_n(v) = \frac{1}{\alpha_n(v) + \beta_n(v)}. \tag{5.15}$$

At elevated potentials $n(t)$ increases monotonically and exponentially toward its resting value, thereby turning on, or *activating*, the K^+ current. Since the Nernst potential is below the resting potential, the K^+ current is an outward current at potentials greater than rest. The function $n(t)$ is called the K^+ *activation*.

It is instructive to consider in detail how such a formulation for g_K results in the required sigmoidal increase and exponential decrease. Suppose that at time $t = 0$, v is increased from 0 to v_0 and then held constant, and suppose further that n is at steady state when $t = 0$, i.e., $n(0) = n_\infty(0)$. For simplicity, we assume that $n_\infty(0) = 0$, although this assumption is not necessary for the argument. Solving (5.12) then gives

$$n(t) = n_\infty(v_0)\left[1 - \exp\left(\frac{-t}{\tau_n(v_0)}\right)\right], \tag{5.16}$$

which is an increasing curve (with monotonically decreasing slope) that approaches its maximum at $n_\infty(v_0)$. Raising n to the fourth power gives a sigmoidally increasing curve as required. Higher powers of n result in curves with a greater maximum slope at the point of inflection. However, in response to a step decrease in v, from v_0 to 0 say, the solution for n is

$$n(t) = n_\infty(v_0)\exp\left(\frac{-t}{\tau_n(0)}\right), \tag{5.17}$$

in which case n^4 is exponentially decreasing, with no inflection point.

It remains to describe how the functions n_∞ and τ_n are determined from the experimental data. For any given voltage step, the time constant τ_n, and the final value of n, namely n_∞, can be determined by fitting (5.16) to the experimental data. By this procedure one can determine τ_n and n_∞ at a discrete set of values for v, i.e., those values used experimentally. Typical data points for n_∞ are shown in Fig. 5.4 as symbols. To obtain a complete description of g_K, valid for all voltages and not only those used in the experiments, Hodgkin and Huxley fitted a smooth curve through the data points. The functional form of the smooth curve has no physiological significance, but is a convenient way of providing a continuous description of n_∞. A similar procedure is followed for τ_n. The continuous descriptions of n_∞ and τ_n (expressed in terms of α_n and β_n) are given in (5.28) and (5.29) below.

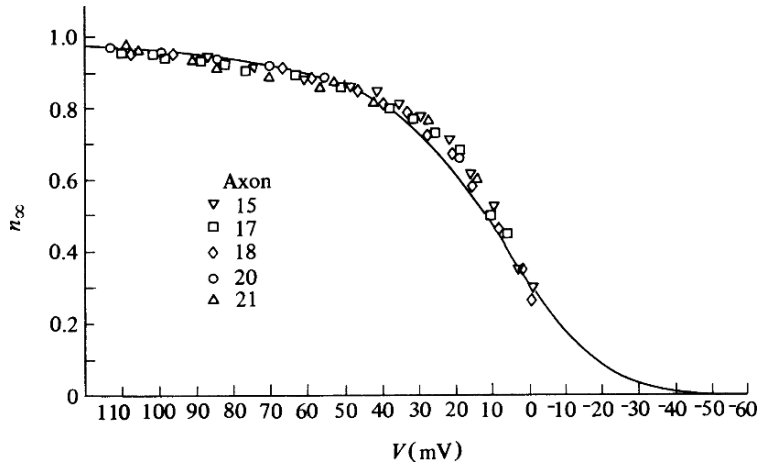

Figure 5.4 Data points (symbols) of n_∞, determined by fitting (5.16) to the experimental time courses. The smooth curve through the symbols provides a continuous description of n_∞, and its functional form has no physiological significance. In the original plot (Hodgkin and Huxley, 1952d, Fig. 5) V was calculated with a reverse sign, which has here been changed to agree with modern conventions. Thus, the horizontal axis appears reversed.

The Sodium Conductance

The time dependence for the Na^+ conductance is more difficult to unravel. From the experimental data it is suggested that there are two processes at work, one that turns on the Na^+ current and one that turns it off. Hodgkin and Huxley proposed that the Na^+ conductance is of the form

$$g_{\mathrm{Na}}(v) = \bar{g}_{\mathrm{Na}} m^3 h, \tag{5.18}$$

and they fitted the time-dependent behavior of m and h to exponentials with dynamics

$$\frac{dw}{dt} = \alpha_w(1 - w) - \beta_w w, \tag{5.19}$$

where $w = m$ or h. Because m is small at rest and first increases, it is called the *sodium activation* variable, and because h shuts down, or inactivates, the Na^+ current, it is called the *sodium inactivation* variable. When $h = 0$, the Na^+ current is completely inactivated. The overall procedure is similar to that used in the specification of g_{K}. For any fixed voltage step, the unknown functions α_w and β_w are determined by fitting to the experimental curves (Fig. 5.3C), and then smooth curves, with arbitrary functional forms, are fitted through the data points for α_w and β_w.

Summary of the Equations

In summary, the Hodgkin–Huxley equations for the space-clamped axon are

$$C_m \frac{dv}{dt} = -\bar{g}_{\mathrm{K}} n^4 (v - v_{\mathrm{K}}) - \bar{g}_{\mathrm{Na}} m^3 h (v - v_{\mathrm{Na}}) - \bar{g}_{\mathrm{L}} (v - v_{\mathrm{L}}) + I_{\mathrm{app}}, \tag{5.20}$$

$$\frac{dm}{dt} = \alpha_m(1-m) - \beta_m m, \tag{5.21}$$

$$\frac{dn}{dt} = \alpha_n(1-n) - \beta_n n, \tag{5.22}$$

$$\frac{dh}{dt} = \alpha_h(1-h) - \beta_h h. \tag{5.23}$$

The specific functions α and β proposed by Hodgkin and Huxley are, in units of $(\text{ms})^{-1}$,

$$\alpha_m = 0.1\,\frac{25-v}{\exp\left(\frac{25-v}{10}\right)-1}, \tag{5.24}$$

$$\beta_m = 4\,\exp\left(\frac{-v}{18}\right), \tag{5.25}$$

$$\alpha_h = 0.07\,\exp\left(\frac{-v}{20}\right), \tag{5.26}$$

$$\beta_h = \frac{1}{\exp\left(\frac{30-v}{10}\right)+1}, \tag{5.27}$$

$$\alpha_n = 0.01\,\frac{10-v}{\exp\left(\frac{10-v}{10}\right)-1}, \tag{5.28}$$

$$\beta_n = 0.125\,\exp\left(\frac{-v}{80}\right). \tag{5.29}$$

For these expressions, the potential v is the deviation from rest ($v = V - V_{\text{eq}}$), measured in units of mV, current density is in units of $\mu\text{A/cm}^2$, conductances are in units of mS/cm^2, and capacitance is in units of $\mu\text{F/cm}^2$. The remaining parameters are

$$\bar{g}_{\text{Na}} = 120, \qquad \bar{g}_{\text{K}} = 36, \qquad \bar{g}_{\text{L}} = 0.3, \qquad C_m = 1, \tag{5.30}$$

with (shifted) equilibrium potentials $v_{\text{Na}} = 115, v_{\text{K}} = -12$, and $v_{\text{L}} = 10.6$. (The astute reader will notice immediately that these values are not quite consistent with the values given in Table 2.1. Instead, these correspond to $V_{\text{Na}} = 50$ mV, $V_{\text{K}} = -77$ mV, $V_{\text{L}} = -54.4$ mV, with an equilibrium membrane potential of $V_{\text{eq}} = -65$ mV. These values are close enough to those of Table 2.1 to be of no concern.) In Fig. 5.5 are shown the steady-state functions and the time constants.

In Chapter 3 we discussed simple models of the gating of Na^+ and K^+ channels and showed how the rate constants in simple kinetic schemes could be determined from whole-cell or single-channel data. We also showed how models of the form (5.20)–(5.23) can be derived by modeling the ionic channels as consisting of multiple subunits, each of which obeys a simple two-state model. For example, the Hodgkin–Huxley Na^+ gating equations can be derived from the assumption that the Na^+ channel consists of three "m" gates and one "h" gate, each of which can be either closed or open. If the gates operate independently, then the fraction of open Na^+ channels is m^3h, where m and h obey the equation of the two-state channel model. Similarly, if there are four "n" gates

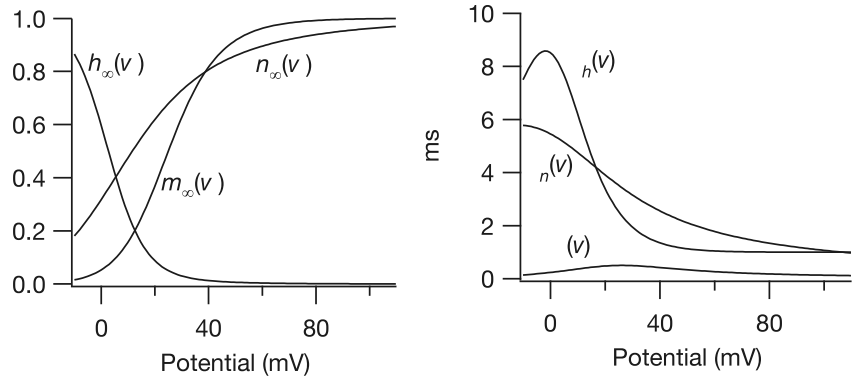

Figure 5.5 In the left panel are the steady-state functions, and in the right panel are the time constants of the Hodgkin–Huxley equations (5.20)–(5.23).

per K^+ channel, all of which must be open for K^+ to flow, then the fraction of open K^+ channels is n^4.

Now comes the most interesting challenge facing these equations. Having incorporated the measurements of conductance found from voltage-clamp experiments, one wonders whether these equations reproduce a realistic action potential, and if so, by what mechanism is the action potential produced? We can describe in qualitative terms how the Hodgkin–Huxley equations should work. If small currents are applied to a cell for a short period of time, the potential returns rapidly to its equilibrium $v = 0$ after the applied current is removed. The equilibrium potential is close to the K^+ Nernst potential $v_K = -12$, because at rest, the Na^+ and leakage conductances are small. There is always competition among the three ionic currents to drive the potential to the corresponding resting potential. For example, if the K^+ and leakage currents could be blocked or the Na^+ conductance dramatically increased, then the term $g_{Na}(V - V_{Na})$ should dominate (5.2), and as long as v is below v_{Na}, an inward Na^+ current would drive the potential toward v_{Na}. Similarly, while v is above v_K, the K^+ current is outward in an attempt to drive v toward v_K. Notice that since $v_K < v_L < v_{Na}$, v is necessarily restricted to lie in the range $v_K < v < v_{Na}$.

If g_{Na} and g_K were constant, that would be the end of the story. The equilibrium at $v = 0$ would be a stable equilibrium, and, following any stimulus, the potential would return exponentially to rest. But since g_{Na} and g_K can change, the different currents can exert their respective influences. The actual sequence of events is determined by the dynamics of m, n, and h. The most important observation for the moment is that $\tau_m(v)$ is much smaller than either $\tau_n(v)$ or $\tau_h(v)$, so that $m(t)$ responds much more quickly to changes in v than either n or h. We can now understand why the Hodgkin–Huxley system is an excitable system. As noted above, if the potential v is raised slightly by a small stimulating current, the system returns to its stable equilibrium. However, during the period of time that the potential v is elevated, the Na^+ activation m tracks $m_\infty(v)$. If the stimulating current is large enough to raise the potential and therefore $m_\infty(v)$ to a

high enough level (above its threshold), then before the system can return to rest, m will increase sufficiently to change the sign of the net current, resulting in an autocatalytic inward Na^+ current. Now, as the potential rises, m continues to rise, and the inward Na^+ current is increased, further adding to the rise of the potential.

If nothing further were to happen, the potential would be driven to a new equilibrium at v_{Na}. However, here is where the difference in time constants plays an important role. When the potential is at rest, the Na^+ inactivation variable, h, is positive, about 0.6. As the potential increases, h_∞ decreases toward zero, and as h approaches zero, the Na^+ current is inactivated because g_{Na} approaches zero. However, because the time constant $\tau_h(v)$ is much larger than $\tau_m(v)$, there is a considerable delay between turning on the Na^+ current (as m increases) and turning off the Na^+ current (as h decreases). The net effect of the two different time scales of m and h is that the Na^+ current is at first turned on and later turned off, and this is seen as an initial increase of the potential, followed by a decrease toward rest.

At about the same time that the Na^+ current is inactivated, the outward K^+ current is activated. This is because of the similarity of the time constants $\tau_n(v)$ and $\tau_h(v)$. Activation of the K^+ current drives the potential below rest toward v_K. When v is negative, n declines, and the potential eventually returns to rest, and the whole process can start again. Fig. 5.6A shows a plot of the potential $v(t)$ during an action potential following a superthreshold stimulus. Fig. 5.6B shows $m(t)$, $n(t)$, and $h(t)$ during the same action potential.

There are four recognizable phases of an action potential: the *upstroke*, *excited*, *refractory*, and *recovery* phases. The refractory period is the period following the excited phase when additional stimuli evoke no substantial response, even though the potential is below or close to its resting value. There can be no response, since the Na^+ channels are inactivated because h is small. As h gradually returns to its resting value, further responses once again become possible.

Oscillations in the Hodgkin–Huxley Equations

There are two ways that the Hodgkin–Huxley system can be made into an autonomous oscillator. The first is to inject a steady current of sufficient strength, i.e., by increasing I_{app}. Such a current raises the resting potential above the threshold for an action potential, so that after the axon has recovered from an action potential, the potential rises to a superthreshold level at which another action potential is evoked.

In Fig. 5.7A we plot the steady state v (i.e., $V - V_{eq}$) as a function of the applied current, I_{app}. The stable steady state is plotted as a solid line, and an unstable steady state is plotted with a dashed line. As I_{app} increases, so does v, and the steady state is stable for $I_{app} < 9.78$, at which value it loses stability in a subcritical Hopf bifurcation. This bifurcation gives rises to a branch of unstable limit cycle oscillations which bends backwards initially. Unstable limit cycles are drawn with a dashed line, and stable ones with a solid line.

In Fig. 5.7A we also plot the minimum and maximum of the oscillations (i.e., osc min and osc max) as functions of I_{app}. The branch of unstable limit cycles terminates at

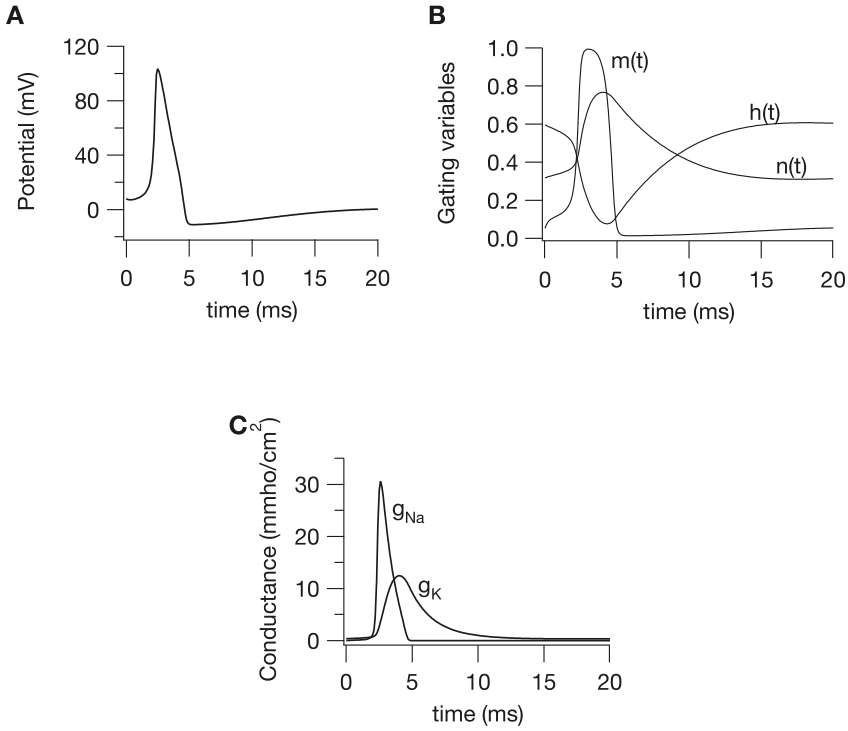

Figure 5.6 An action potential in the Hodgkin–Huxley equations. A: The action potential; B: the gating variables during an action potential, and C: the conductances during an action potential.

a limit point (a saddle-node of periodics, or SNP, bifurcation) where it coalesces with a branch of stable limit cycles. The stable periodic solutions are observed by direct numerical simulation of the differential equations. At larger values of I_{app}, the limit cycles disappear in another Hopf bifurcation, this time a supercritical one, leaving only a branch of stable steady-state solutions for higher values of I_{app}.

Hence, for intermediate values of I_{app}, stable oscillations exist. Two examples are shown in Fig. 5.7B. When I_{app} is too high, the model exhibits only a raised steady state. Furthermore, for a narrow range of values of I_{app}, slightly below the lower Hopf bifurcation, a stable steady state, an unstable periodic orbit, and a stable periodic orbit coexist.

Immersing the axon in a bath of high extracellular K^+ has the same effect through a slightly different mechanism. Increased extracellular K^+ has the effect of increasing the K^+ Nernst potential, raising the resting potential (since the resting potential is close to the K^+ Nernst potential). If this increase of the K^+ Nernst potential is sufficiently large, the resting potential becomes superthreshold, and autonomous oscillations result. This mechanism of creating an autonomous oscillator out of normally excitable but nonoscillatory cells is important for certain cardiac arrhythmias.

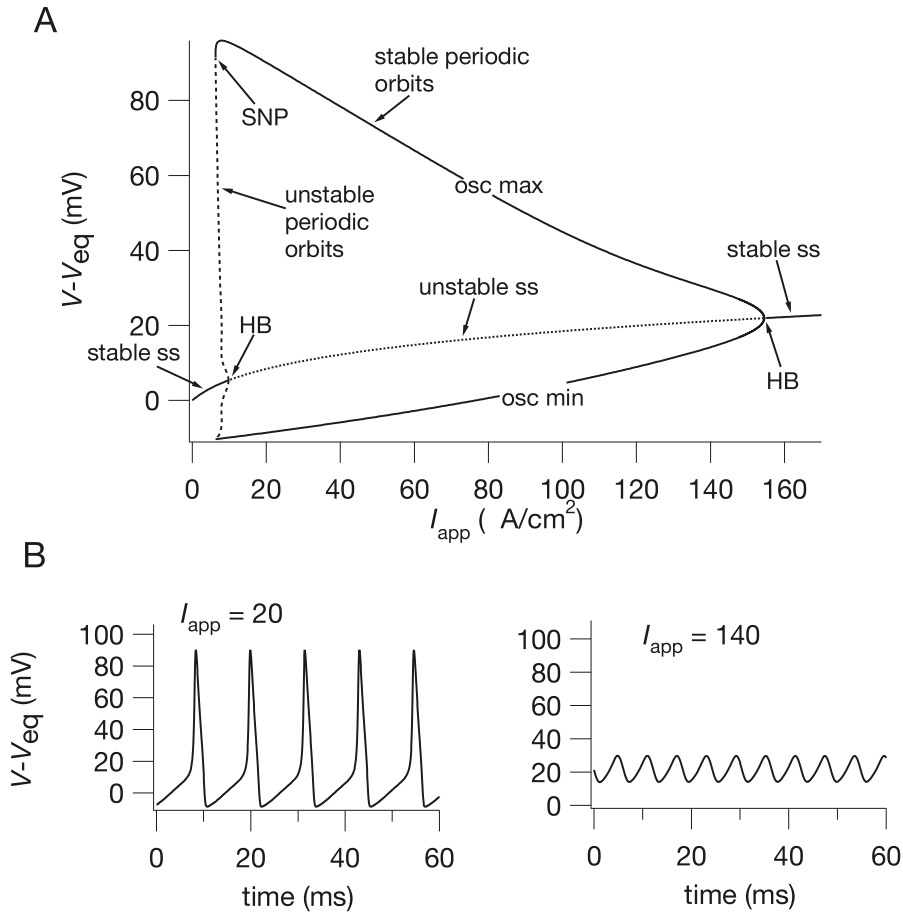

Figure 5.7 A: Bifurcation diagram of the Hodgkin–Huxley equations, with the applied current, I_{app} as the bifurcation parameter. HB denotes a Hopf bifurcation, SNP denotes a saddle-node of periodics bifurcation, osc max and osc min denote, respectively, the maximum and minimum of an oscillation, and ss denotes a steady state. Solid lines denote stable branches, dashed or dotted lines denote unstable branches. B: Sample oscillations at two different values of I_{app}.

5.1.3 Qualitative Analysis

FitzHugh (1960, 1961, 1969) provided a particularly elegant qualitative description of the Hodgkin–Huxley equations that allows a better understanding of the model's behavior. More detailed analyses have also been given by Rinzel (1978), Troy (1978), Cole et al. (1955), and Sabah and Spangler (1970). FitzHugh's approach is based on the fact that some of the model variables have fast kinetics, while others are much slower. In particular, m and v are fast variables (i.e., the Na^+ channel activates quickly, and the membrane potential changes quickly), while n and h are slow variables (i.e.,

Na^+ channels are inactivated slowly, and the K^+ channels are activated slowly). Thus, during the initial stages of the action potential, n and h remain essentially constant while m and v vary. This allows the full four-dimensional phase space to be simplified by fixing the slow variables and considering the behavior of the model as a function only of the two fast variables. Although this description is accurate only for the initial stages of the action potential, it provides a useful way to study the process of excitation.

The Fast Phase Plane

Thus motivated, we fix the slow variables n and h at their respective resting states, which we call n_0 and h_0, and consider how m and v behave in response to stimulation. The differential equations for the fast phase plane are

$$C_m \frac{dv}{dt} = -\bar{g}_K n_0^4 (v - v_K) - \bar{g}_{Na} m^3 h_0 (v - v_{Na}) - \bar{g}_L (v - v_L), \tag{5.31}$$

$$\frac{dm}{dt} = \alpha_m (1 - m) - \beta_m m, \tag{5.32}$$

or, equivalently,

$$\tau_m \frac{dm}{dt} = m_\infty - m. \tag{5.33}$$

This is a two-dimensional system and can be studied in the (m, v) phase plane, a plot of which is given in Fig. 5.8. The curves defined by $dv/dt = 0$ and $dm/dt = 0$ are the v and m nullclines, respectively. The m nullcline is the curve $m = m_\infty(v)$, which we have seen before (in Fig. 5.5), while the v nullcline is the curve

$$v = \frac{\bar{g}_{Na} m^3 h_0 v_{Na} + \bar{g}_K n_0^4 v_K + \bar{g}_L v_L}{\bar{g}_{Na} m^3 h_0 + \bar{g}_K n_0^4 + \bar{g}_L}. \tag{5.34}$$

For the parameters of the Hodgkin–Huxley equations, the m and v nullclines intersect in three places, corresponding to three steady states of the fast equations. Note that these three intersections are not steady states of the full model, only of the fast subsystem, and, to be precise, should be called pseudo-steady states. However, in the context of the fast phase plane we continue to call them steady states. We label the three steady states v_r, v_s, and v_e (for resting, saddle, and excited).

It is left as an exercise to show that v_r and v_e are stable steady states of the fast subsystem, while v_s is a saddle point. Since v_s is a saddle point, it has a one-dimensional stable manifold, shown as a dot-dash line in Fig. 5.8. This stable manifold divides the (m, v) plane into two regions: any trajectory starting to the left of the stable manifold is prevented from reaching v_e and must eventually return to the resting state, v_r. However, any trajectory starting to the right of the stable manifold is prevented from returning to the resting state and must eventually end up at the excited state, v_e. Hence, the stable manifold, in combination with the two stable steady states, gives rise to a threshold phenomenon. Any perturbation from the resting state that is not large enough to cross the stable manifold eventually dies away, but a perturbation that crosses the

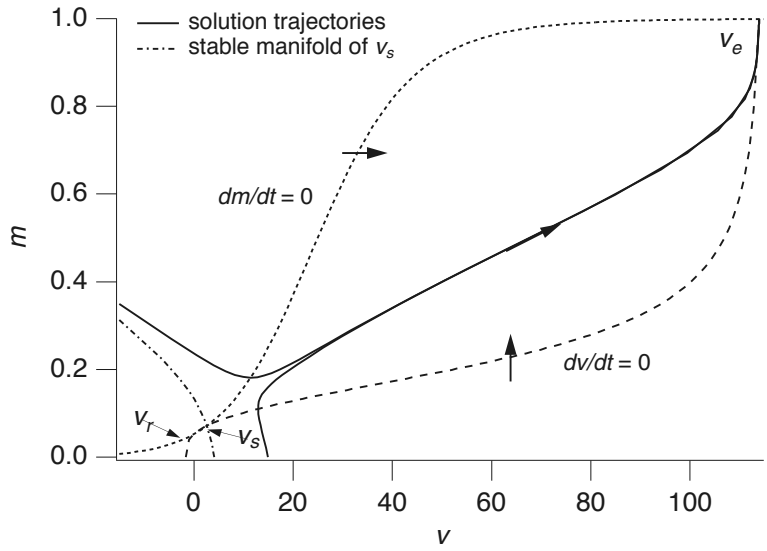

Figure 5.8 The Hodgkin–Huxley fast phase plane, showing the nullclines $dv/dt = 0$ and $dm/dt = 0$ (with $h_0 = 0.596$, $n_0 = 0.3176$), two sample trajectories and the stable manifold of the saddle point v_s.

stable manifold results in a large excursion in the voltage to the excited state. Sample trajectories are sketched in Fig. 5.8.

If m and v were the only variables in the model, then v would stay at v_e indefinitely. However, as pointed out before, v_e is not a steady state of the full model. Thus, to see what happens on a longer time scale, we must consider how slow variations in n and h affect the fast phase plane. First note that since $v_e > v_r$, it follows that $h_\infty(v_e) < h_\infty(v_r)$ and $n_\infty(v_e) > n_\infty(v_r)$. Hence, while v is at the excited state, h begins to decrease, thus inactivating the Na^+ conductance, and n starts to increase thus activating the K^+ conductance. Next note that although the m nullcline in the fast phase plane is independent of n and h, the v nullcline is not. In Fig. 5.8 the nullclines were drawn using the steady-state values for n and h: different values of n and h change the shape of the v nullcline. As n increases and h decreases, the v nullcline moves to the left and up, as illustrated in Fig. 5.9. As the v nullcline moves up and to the left, v_e and v_s move toward each other, while v_r moves to the left. During this phase the voltage is at v_e and thus decreases slowly. Eventually, v_e and v_s coalesce and disappear in a saddle-node bifurcation. When this happens v_r is the only remaining steady state, and so the solution must return to the resting state. Note that since the v nullcline has moved up and to the left, v_r is not a steady state of the full system. However, when v decreases to v_r, n and h both return to their steady states and as they do so, v_r slowly increases until the steady state of the full system is reached and the action potential is complete. A schematic diagram of a complete action potential is shown in Fig. 5.10.

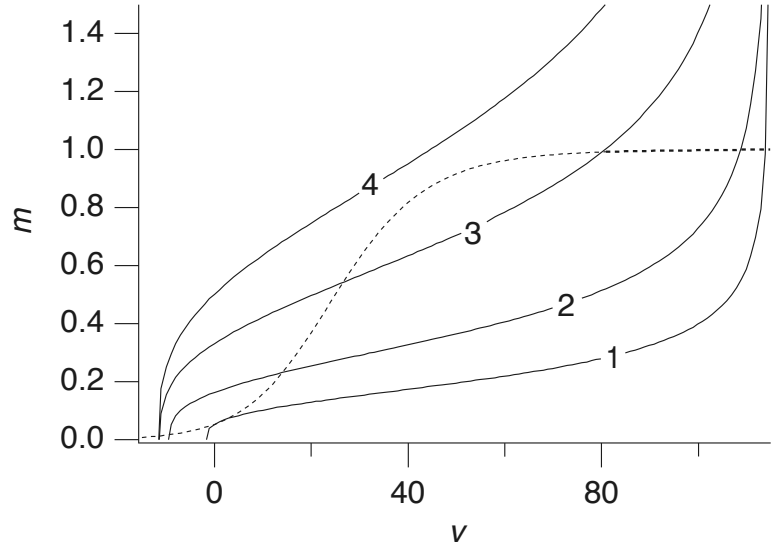

Figure 5.9 The Hodgkin–Huxley fast phase plane as a function of the slow variables, showing the m nullcline (dashed), the movement of the v nullcline (solid) and the disappearance of the steady states. For these curves, parameter values are (1) $h_0 = 0.596$, $n_0 = 0.3176$; (2) $h_0 = 0.4$, $n_0 = 0.5$; (3) $h_0 = 0.2$, $n_0 = 0.7$; and (4) $h_0 = 0.1$, $n_0 = 0.8$.

The Fast–Slow Phase Plane

In the above analysis, the four-dimensional phase space was simplified by taking a series of two-dimensional cross-sections, those with various fixed values of n and h. However, by taking a different cross-section other aspects of the action potential can be highlighted. In particular, by taking a cross-section involving one fast variable and one slow variable we obtain a description of the Hodgkin–Huxley equations that has proven to be extraordinarily useful.

We extract a single fast variable by assuming that m is always in instantaneous equilibrium, and thus $m = m_\infty(v)$. This corresponds to assuming that activation of the Na^+ conductance is on a time scale faster than that of the voltage. Next, FitzHugh noticed that during the course of an action potential, $h+n \approx 0.8$ (notice the approximate symmetry of $n(t)$ and $h(t)$ in Fig. 5.6), and thus h can be eliminated by setting $h = 0.8-n$. With these simplifications, the Hodgkin–Huxley equations contain one fast variable v and one slow variable n, and can be written as

$$-C_m \frac{dv}{dt} = \bar{g}_K n^4 (v - v_K) + \bar{g}_{Na} m_\infty^3(v)(0.8 - n)(v - v_{Na}) + \bar{g}_L (v - v_L), \tag{5.35}$$

$$\frac{dn}{dt} = \alpha_n (1 - n) - \beta_n n. \tag{5.36}$$

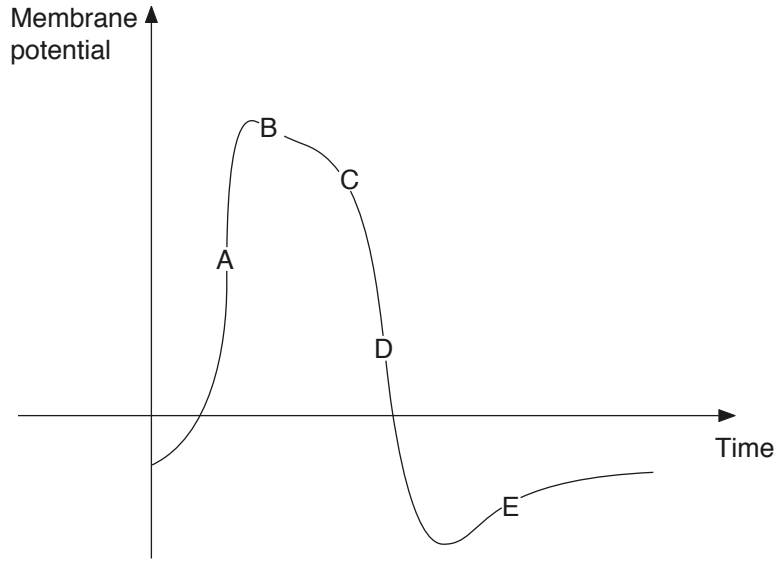

Figure 5.10 Schematic diagram of a complete action potential. A: Superthreshold stimulus causes a fast increase of v to the excited state. B: v is sitting at the excited state, v_e, decreasing slowly as n increases and h decreases, i.e., as v_e moves toward v_s. C: v_e and v_s disappear at a saddle-node bifurcation, and so, D: The solution must return to the resting state v_r. E: n and h slowly return to their resting states, and as they do so, v_r slowly increases until the steady state of the full four-dimensional system is reached.

For convenience we let $f(v,n)$ denote the right-hand side of (5.35), i.e.,

$$-f(v,n) = \bar{g}_{\mathrm{K}} n^4 (v - v_{\mathrm{K}}) + \bar{g}_{\mathrm{Na}} m_\infty^3(v)(0.8 - n)(v - v_{\mathrm{Na}}) + \bar{g}_{\mathrm{L}}(v - v_{\mathrm{L}}). \tag{5.37}$$

A plot of the nullclines of the fast–slow subsystem is given in Fig. 5.11A. The v nullcline is defined by $f(v,n) = 0$ and has a cubic shape, while the n nullcline is $n_\infty(v)$ and is monotonically increasing. There is a single intersection (at least for the given parameter values) and thus a single steady state. Because v is a fast variable and n is a slow one, the solution trajectories are almost horizontal except where $f(v,n) \approx 0$. The curve $f(v,n) = 0$ is called the *slow manifold*. Along the slow manifold the solution moves slowly in the direction determined by the sign of dn/dt, but away from the slow manifold the solution moves quickly in a horizontal direction. From the sign of dv/dt it follows that the solution trajectories move away from the middle branch of the slow manifold and toward the left and right branches. Thus, the middle branch is termed the unstable branch of the slow manifold. This unstable branch acts as a threshold. If a perturbation from the steady state is small enough so that v does not cross the unstable manifold, then the trajectory moves horizontally toward the left and returns to the steady state. However, if the perturbation is large enough so that v crosses the unstable manifold, then the trajectory moves to the right until it reaches

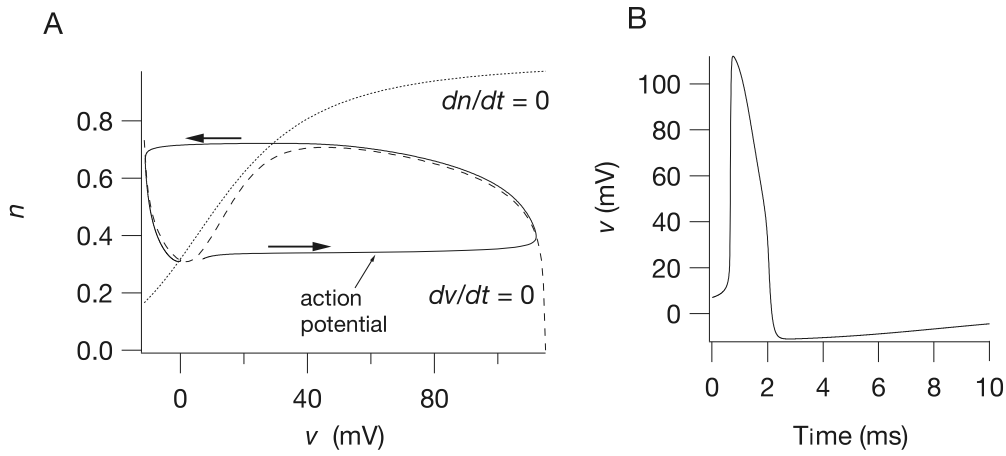

Figure 5.11 A: Fast–slow phase plane of the Hodgkin–Huxley equations (with $I_{\text{app}} = 0$), showing the nullclines and an action potential. B: Action potential of panel A, plotted as a function of time.

the right branch of the slow manifold, which corresponds to the excited state. On this right branch $dn/dt > 0$, and so the solution moves slowly up the slow manifold until the turning point is reached. At the turning point, n cannot increase any further, as the right branch of the slow manifold ceases to exist, and so the solution moves over to the left branch of the slow manifold. On this left branch $dn/dt < 0$, and so the solution moves down the left branch until the steady state is reached, completing the action potential (Fig. 5.11A). A plot of the potential as a function of time is shown in Fig. 5.11B.

The variables v and n are usually called the excitation and recovery variables, respectively: excitation because v governs the rise to the excited state, and recovery because n causes the return to the steady state. In the absence of n the solution would stay at the excited state indefinitely.

There is a close relationship between the fast phase plane and the fast–slow phase plane. Recall that in the fast phase plane, the v and m nullclines have three intersection points when $n = n_0$ and $h = h_0$. These three intersections correspond to the three branches of the curve $f(v, n_0) = 0$. In other words, when n is fixed at n_0, the equation $f(v, n_0) = 0$ has three possible solutions, corresponding to v_r, v_s and v_e in the fast phase plane. However, consideration of Fig. 5.11 shows that, as n increases, the two rightmost branches of the slow manifold (i.e., the dashed line) coalesce and disappear. This is analogous to the merging and disappearance of v_e and v_s seen in the fast phase plane (Fig. 5.9). The fast–slow phase plane is a convenient way of summarizing how v_r, v_s, and v_e depend on the slow variables.

This representation of the Hodgkin–Huxley equations in terms of two variables, one fast and one slow, is the basis of the FitzHugh–Nagumo model of excitability, and models of this generic type are discussed in some detail throughout this book.

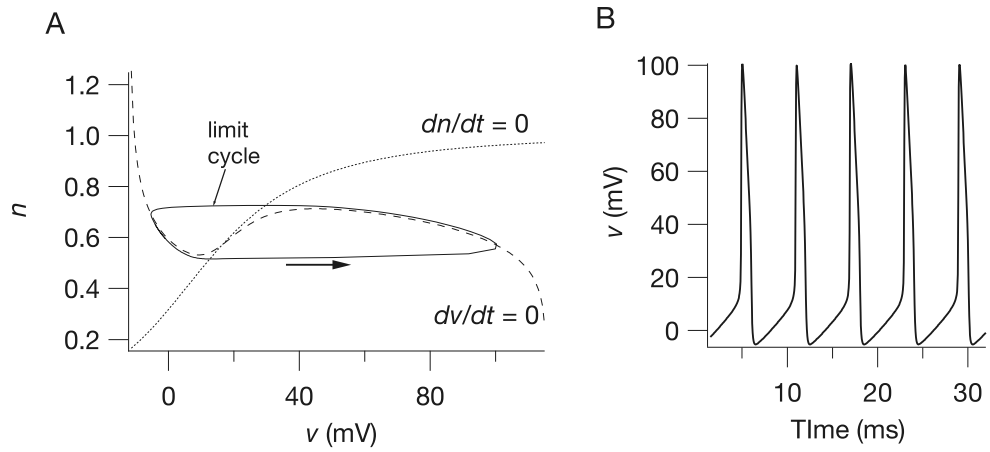

Figure 5.12 A: Fast–slow phase plane of the Hodgkin–Huxley equations, with $I_{app} = 50$, showing the nullclines and an oscillation. B: The oscillations of panel A, plotted as a function of time.

Oscillations in the Fast–Slow Phase Plane

As was true for the full Hodgkin–Huxley equations, the addition of an applied current to the fast–slow phase plane gives rise to oscillations. Why this is so can be seen in Fig. 5.12. As I_{app} increases, the cubic nullcline moves across and up, until the two nullclines intersect on the middle branch of the cubic. The trajectory can never approach this steady state, always falling off each of the branches of the cubic, and alternating periodically between the two stable branches in what is called a relaxation limit cycle.

5.2 The FitzHugh–Nagumo Equations

There is considerable value in studying systems of equations that are simpler than the Hodgkin–Huxley equations but that retain many of their qualitative features. This is the motivation for the FitzHugh–Nagumo equations and their variants. Basically, the FitzHugh–Nagumo equations extract the essential behavior of the Hodgkin–Huxley fast–slow phase plane and presents it in a simplified form. Thus, the FitzHugh–Nagumo equations have two variables, one fast (v) and one slow (w). The fast variable has a cubic nullcline and is called the excitation variable, while the slow variable is called the recovery variable and has a nullcline that is monotonically increasing. The nullclines have a single intersection point, which, without loss of generality, is assumed to be at the origin. A schematic diagram of the phase plane is given in Fig. 5.13, where we introduce some of the notation used later in this section.

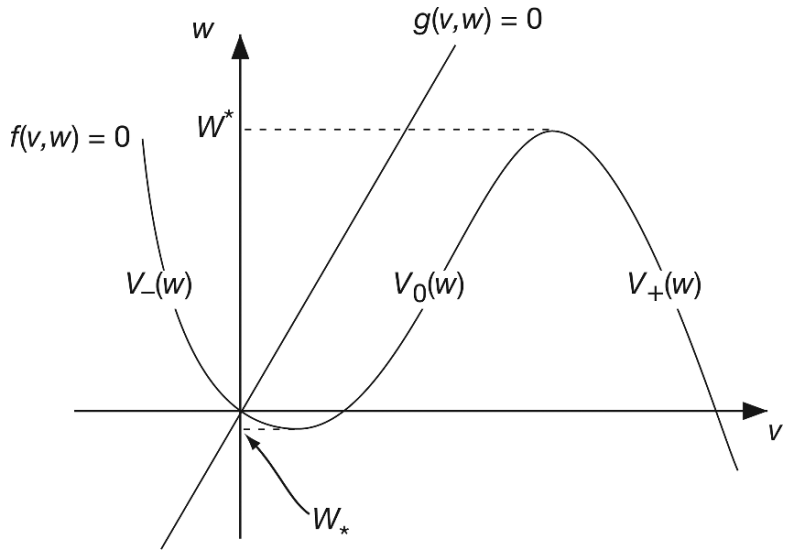

Figure 5.13 Schematic diagram of the generalized FitzHugh–Nagumo phase plane.

The traditional FitzHugh–Nagumo equations are obtained by assuming a cubic nullcline for v and a linear nullcline for w. Thus,

$$\epsilon \frac{dv}{dt} = f(v) - w + I_{\text{app}}, \tag{5.38}$$

$$\frac{dw}{dt} = v - \gamma w, \tag{5.39}$$

where

$$f(v) = v(1-v)(v-\alpha), \qquad \text{for } 0 < \alpha < 1, \epsilon \ll 1. \tag{5.40}$$

I_{app} is the applied current. Typical values would be $\alpha = 0.1$, $\gamma = 0.5$ and $\epsilon = 0.01$.

Other choices for $f(v)$ include the McKean model (McKean, 1970), for which

$$f(v) = H(v-\alpha) - v, \tag{5.41}$$

where H is the Heaviside function. This choice recommends itself because then the model is piecewise linear, allowing explicit solutions of many interesting problems. Another piecewise-linear model (also proposed by McKean, 1970) has

$$f(v) = \begin{cases} -v, & \text{for} \quad v < \alpha/2, \\ v - \alpha, & \text{for} \quad \frac{\alpha}{2} < v < \frac{1+\alpha}{2}, \\ 1 - v, & \text{for} \quad v > \frac{1+\alpha}{2}. \end{cases} \tag{5.42}$$

A third piecewise-linear model that has found widespread usage is the *Pushchino* model, so named because of its development in Pushchino (about 70 miles south of

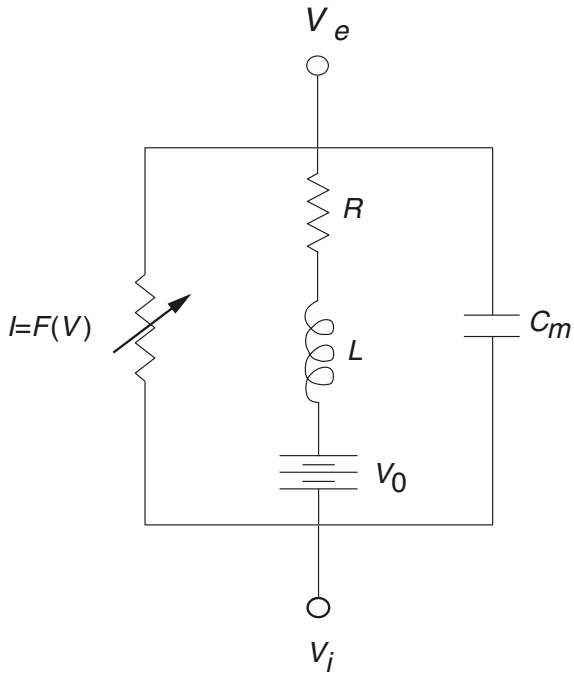

Figure 5.14 Circuit diagram for the FitzHugh–Nagumo equations.

Moscow), by Krinsky, Panfilov, Pertsov, Zykov, and their coworkers. The details of the Pushchino model are described in Exercise 13.

The FitzHugh–Nagumo equations can be derived from a simplified model of the cell membrane (Fig. 5.14). Here the cell (or membrane patch) consists of three components, a capacitor representing the membrane capacitance, a nonlinear current–voltage device for the fast current, and a resistor, inductor, and battery in series for the recovery current. In the 1960s Nagumo, a Japanese electrical engineer, built this circuit using a tunnel diode as the nonlinear element (Nagumo et al., 1964), thereby attaching his name to this system.

Using Kirchhoff's laws, we can write down equations for the behavior of this membrane circuit diagram. We find

$$C_m \frac{dV}{d\tau} + F(V) + i = -I_0, \tag{5.43}$$

$$L\frac{di}{d\tau} + Ri = V - V_0, \tag{5.44}$$

where I_0 is the applied external current, i is the current through the resistor–inductor, $V = V_i - V_e$ is the membrane potential, and V_0 is the potential gain across the battery. Here τ is used to represent dimensional time because we shortly introduce t as a dimensionless time variable. The function $F(V)$ is assumed to be of cubic shape, having three zeros, of which the smallest $V = 0$ and largest $V = V_1$ are stable solutions of the differential equation $dV/d\tau = -F(V)$. We take R_1 to be the passive resistance of

the nonlinear element, $R_1 = 1/F'(0)$. Now we introduce the dimensionless variables $v = V/V_1, w = R_1 i/V_1, f(v) = -R_1 F(V_1 v)/V_1$, and $t = L\tau/R_1$. Then (5.43) and (5.44) become

$$\epsilon \frac{dv}{dt} = f(v) - w - w_0, \tag{5.45}$$

$$\frac{dw}{dt} = v - \gamma w - v_0, \tag{5.46}$$

where $\epsilon = R_1^2 C_m/L, w_0 = R_1 I_0/V_1, v_0 = V_0/V_1$, and $\gamma = R/R_1$.

An important variant of the FitzHugh–Nagumo equations is the *van der Pol oscillator*. An electrical engineer, van der Pol built the circuit using triodes because it exhibits stable oscillations. As there was little interest in oscillatory circuits at the time, he proposed his circuit as a model of an oscillatory cardiac pacemaker (van der Pol and van der Mark, 1928). Since then it has become a classic example of a system with limit cycle behavior and relaxation oscillations, included in almost every textbook on oscillations (see, for example, Stoker, 1950, or Minorsky, 1962).

If we eliminate the resistor R from the circuit in Fig. 5.14, differentiate (5.43), and eliminate the current i, we get the second-order differential equation

$$C_m \frac{d^2V}{d\tau^2} + F'(V)\frac{dV}{d\tau} + \frac{V}{L} = \frac{V_0}{L}. \tag{5.47}$$

Following rescaling, and setting $F(v) = A(v^3/3 - v)$, we arrive at the *van der Pol equation*

$$v'' + a(v^2 - 1)v' + v = 0. \tag{5.48}$$

5.2.1 The Generalized FitzHugh-Nagumo Equations

From now on, by the *generalized FitzHugh–Nagumo equations* we mean the system of equations

$$\epsilon \frac{dv}{dt} = f(v, w), \tag{5.49}$$

$$\frac{dw}{dt} = g(v, w), \tag{5.50}$$

where the nullcline $f(v, w) = 0$ is of "cubic" shape. By this we mean that for a finite range of values of w, there are three solutions $v = v(w)$ of the equation $f(v, w) = 0$. These we denote by $v = V_-(w), v = V_0(w)$, and $v = V_+(w)$, and, where comparison is possible (since these functions need not all exist for the same range of w),

$$V_-(w) \le V_0(w) \le V_+(w). \tag{5.51}$$

We denote the minimal value of w for which $V_-(w)$ exists by W_*, and the maximal value of w for which $V_+(w)$ exists by W^*. For values of w above the nullcline $f(v, w) = 0, f(v, w) < 0$, and below the nullcline, $f(v, w) > 0$ (in other words, $f_w(v, w) < 0$).

The nullcline $g(v, w) = 0$ is assumed to have precisely one intersection with the curve $f(v, w) = 0$. Increasing v beyond the curve $g(v, w) = 0$ makes $g(v, w)$ positive

(i.e., $g_v(v,w) > 0$), and decreasing w below the curve $g(v,w) = 0$ increases $g(v,w)$ (hence $g_w(v,w) < 0$). The nullclines f and g are illustrated in Fig. 5.13.

5.2.2 Phase-Plane Behavior

One attractive feature of the FitzHugh–Nagumo equations is that because they form a two-variable system, they can be studied using phase-plane techniques. (For an example of a different approach, see Troy, 1976.) There are two characteristic phase portraits possible (shown in Figs. 5.15 and 5.16). By assumption, there is only one steady state, at $v = v^*, w = w^*$, with $f(v^*, w^*) = g(v^*, w^*) = 0$. Without loss of generality, we assume that this steady state occurs at the origin, as this involves only a shift of the variables. Furthermore, it is typical that the parameter ϵ is a small number. For small ϵ, if the steady state lies on either the left or right solution branch of $f(v,w) = 0$, i.e., the curves $v = V_{\pm}(w)$, it is linearly stable. Somewhere on the middle solution branch $v = V_0(w)$, near the extremal values of the curve $f(v,w) = 0$, there is a Hopf bifurcation point. If parameters are varied so that the steady-state solution passes through this point, a periodic orbit arises as a continuous solution branch and bifurcates into a stable limit cycle oscillation.

When the steady state is on the leftmost branch, but close to the minimum (Fig. 5.15), the system is excitable. This is because even though the steady state is

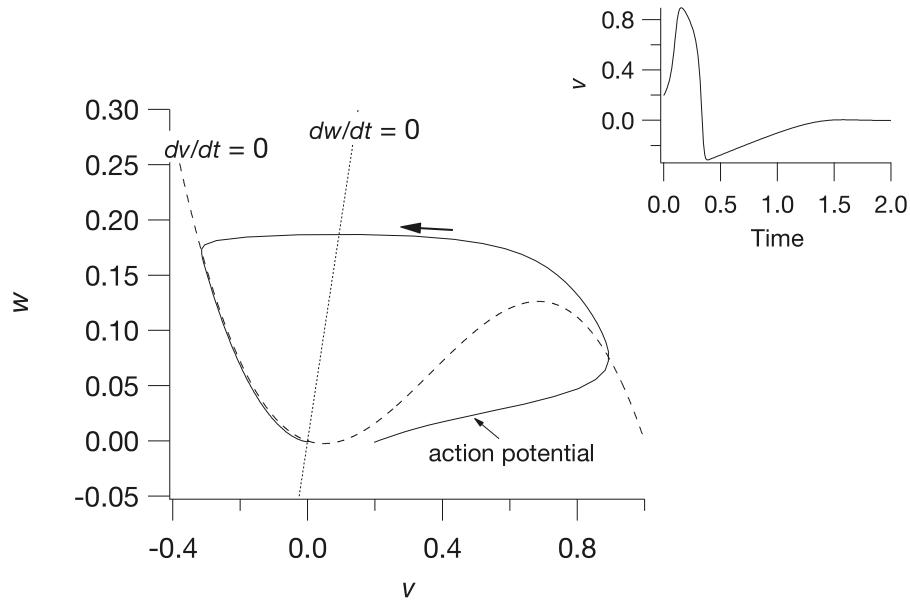

Figure 5.15 Phase portrait for the FitzHugh–Nagumo equations, (5.38)–(5.40), with $\alpha = 0.1$, $\gamma = 0.5$, $\epsilon = 0.01$ and zero applied current. For these parameter values the system has a unique globally stable rest point, but is excitable. The inset at top right shows the action potential as a function of time.

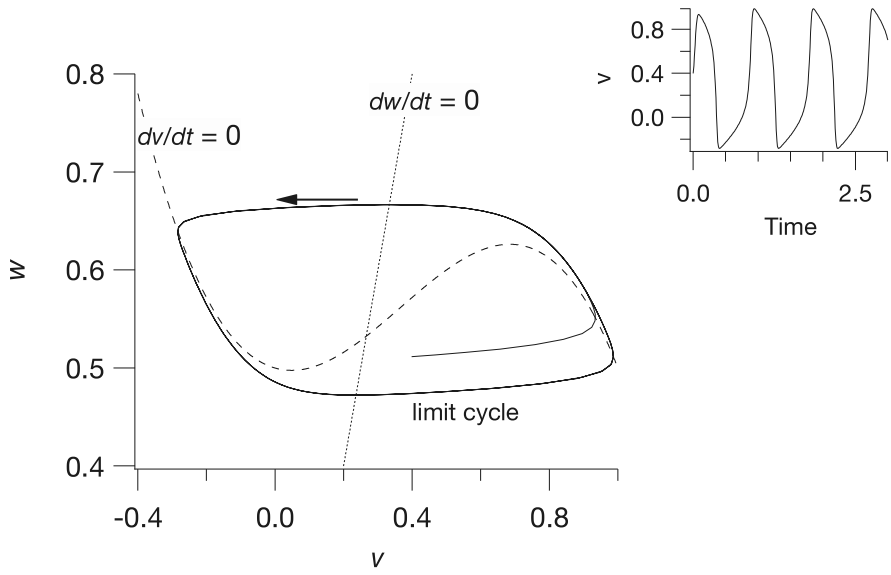

Figure 5.16 Phase portrait for the FitzHugh–Nagumo equations, (5.38)–(5.40), with $\alpha = 0.1$, $\gamma = 0.5$, $\epsilon = 0.01$ and $I_{\text{app}} = 0.5$. For these parameter values, the unique rest point is unstable and there is a globally stable periodic orbit. The inset at top right shows the periodic orbit plotted against time.

linearly stable, a sufficiently large perturbation from the steady state sends the state variable on a trajectory that runs away from the steady state before eventually returning to rest. Such a trajectory goes rapidly to the rightmost branch, which it hugs as it gradually creeps upward, where upon reaching the maximum, it goes rapidly to the leftmost branch and then gradually returns to rest, staying close to this branch as it does. Plots of the variables v and w are shown as functions of time in Fig. 5.15.

The mathematical description of these events follows from singular perturbation theory. With $\epsilon \ll 1$, the variable v is a fast variable and the variable w is a slow variable. This means that if possible, v is adjusted rapidly to maintain a pseudo-equilibrium at $f(v, w) = 0$. In other words, if possible, v clings to the stable branches of $f(v, w) = 0$, namely $v = V_{\pm}(w)$. Along these branches the dynamics of w are governed by the reduced dynamics

$$\frac{dw}{dt} = g(V_{\pm}(w), w) = G_{\pm}(w). \tag{5.52}$$

When it is not possible for v to be in quasi-equilibrium, the motion is governed approximately by the differential equations,

$$\frac{dv}{d\tau} = f(v, w), \qquad \frac{dw}{d\tau} = 0, \tag{5.53}$$

found by making the change of variables to the fast time scale $t = \epsilon\tau$, and then setting $\epsilon = 0$. On this time scale, w is constant, while v equilibrates to a stable solution of $f(v, w) = 0$.

The evolution of v and w starting from specified initial conditions v_0 and w_0 can now be described. Suppose v_0 is greater than the rest value v^*. If $v_0 < V_0(w)$, then v returns directly to the steady state. If $v_0 > V_0(w)$, then v goes rapidly to the upper branch $V_+(w)$ with w remaining nearly constant at w_0. The curve $v = V_0(w)$ is a *threshold curve*. While v remains on the upper branch, w increases according to

$$\frac{dw}{dt} = G_+(w), \tag{5.54}$$

as long as possible. However, in the finite time

$$T_e = \int_{w_0}^{W^*} \frac{dw}{G_+(w)}, \tag{5.55}$$

w reaches the "knee" of the nullcline $f(v, w) = 0$. This period of time constitutes the *excited phase* of the action potential.

When w reaches W^* it is no longer possible for v to stay on the excited branch, so it must return to the lower branch $V_-(w)$. Once on this branch, w decreases following the dynamics

$$\frac{dw}{dt} = G_-(w). \tag{5.56}$$

If the rest point lies on the lower branch, then $G_-(w^*) = 0$, and w gradually returns to rest on the lower branch.

Applied Current and Oscillations

When a current is applied to the generalized FitzHugh–Nagumo equations, they become

$$\epsilon\frac{dv}{dt} = f(v, w) + I_{\text{app}}, \tag{5.57}$$

$$\frac{dw}{dt} = g(v, w). \tag{5.58}$$

As with the fast–slow phase plane of the Hodgkin–Huxley equations, the cubic nullcline moves up as I_{app} increases. Thus, when I_{app} takes values in some intermediate range, the steady state lies on the middle branch, $V_0(w)$, and is unstable. Instead of returning to rest after one excursion on the excited branch, the trajectory alternates periodically between the upper and lower branches, with w varying between W_* and W^* (Fig. 5.16). This limit cycle behavior, where there are fast jumps between regions in which the solution moves more slowly, is called a *relaxation oscillation*. In this figure, the relaxation nature of the oscillations is not very pronounced; however, as ϵ decreases, the jumps

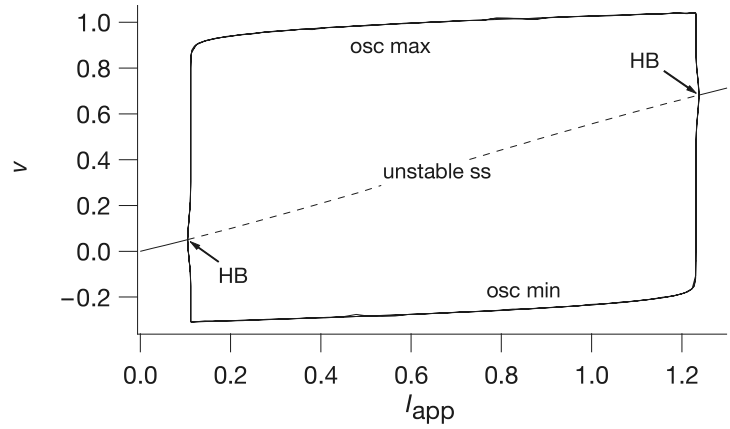

Figure 5.17 Bifurcation diagram of the FitzHugh–Nagumo equations, (5.38)–(5.40), with $\alpha = 0.1$, $\gamma = 0.5$, $\epsilon = 0.01$, with the applied current as the bifurcation parameter. The steady-state solution is labeled ss, while osc max and osc min denote, respectively, the maximum and minimum of v over an oscillation. HB denotes a Hopf bifurcation point.

become faster. For small ϵ, the period of the oscillation is approximately

$$T = \int_{W_*}^{W^*} \left(\frac{1}{G_+(w)} - \frac{1}{G_-(w)} \right) dw. \tag{5.59}$$

This number is finite because $G_+(w) > 0$, and $G_-(w) < 0$ for all appropriate w.

As with the Hodgkin–Huxley equations, the behavior of the periodic orbits as I_{app} varies can be summarized in a bifurcation diagram. For each value of I_{app} we plot the value of v at the steady state, and (where appropriate) the maximum and minimum values of v over a periodic orbit. As I_{app} increases, a branch of periodic orbits appears in a Hopf bifurcation at $I_{\text{app}} = 0.1$ and disappears again in another Hopf bifurcation at $I_{\text{app}} = 1.24$. Between these two points there is a branch of stable periodic orbits. The bifurcation diagram is shown in Fig. 5.17.

5.3 EXERCISES

1. Show that, if $k > 1$, then $(1 - e^{-x})^k$ has an inflection point, but $(e^{-x})^k$ does not.

2. Explain why replacing the extracellular Na^+ with choline has little effect on the resting potential of an axon. Calculate the new resting potential with 90% of the extracellular Na^+ removed. Why is the same not true if K^+ is replaced? (Assume the conductances are constant.)

3. Plot the nullclines of the Hodgkin–Huxley fast subsystem. Show that v_r and v_e in the Hodgkin–Huxley fast subsystem are stable steady states, while v_s is a saddle point. Compute the stable manifold of the saddle point and compute sample trajectories in the fast phase plane, demonstrating the threshold effect.

4. Show how the Hodgkin–Huxley fast subsystem depends on the slow variables; i.e., show how the v nullcline moves as n and h are changed, and demonstrate the saddle-node bifurcation in which v_e and v_s disappear.

5. Plot the nullclines of the fast–slow Hodgkin–Huxley phase plane and compute a complete action potential.

6. How does the phase plane of the fast–slow Hodgkin–Huxley equations change with applied current? How much applied current in the fast–slow Hodgkin–Huxley equations is needed to generate oscillations? Plot a typical oscillation in the phase plane. Plot the maximum of the oscillation against the applied current to construct a bifurcation diagram.

7. Suppose that in the Hodgkin–Huxley fast–slow phase plane, v is slowly decreased to $v^* < v_0$ (where v_0 is the steady state), held there for a considerable time, and then released. Describe what happens in qualitative terms, i.e., without actually computing the solution. This is called *anode break excitation* (Hodgkin and Huxley, 1952d. Also see Peskin, 1991). What happens if v is instantaneously decreased to v^* and then released immediately? Why do these two solutions differ?

8. In the text, the Hodgkin–Huxley equations are written in terms of $v = V - V_{\text{eq}}$. Show that in terms of V the equations are

$$C_m \frac{dV}{dt} = -\bar{g}_{\text{K}} n^4 (V - V_{\text{K}}) - \bar{g}_{\text{Na}} m^3 h (V - V_{\text{Na}}) - \bar{g}_{\text{L}} (V - V_{\text{L}}) + I_{\text{app}}, \tag{5.60}$$

$$\frac{dm}{dt} = \alpha_m (1 - m) - \beta_m m, \tag{5.61}$$

$$\frac{dn}{dt} = \alpha_n (1 - n) - \beta_n n, \tag{5.62}$$

$$\frac{dh}{dt} = \alpha_h (1 - h) - \beta_h h, \tag{5.63}$$

where (in units of $(\text{ms})^{-1}$),

$$\alpha_m = 0.1 \frac{-40 - V}{\exp\left(\frac{-40-V}{10}\right) - 1}, \tag{5.64}$$

$$\beta_m = 4 \exp\left(\frac{-V - 65}{18}\right), \tag{5.65}$$

$$\alpha_h = 0.07 \exp\left(\frac{-V - 65}{20}\right), \tag{5.66}$$

$$\beta_h = \frac{1}{\exp(\frac{-35-V}{10}) + 1}, \tag{5.67}$$

$$\alpha_n = 0.01 \frac{-55 - V}{\exp(\frac{-55-V}{10}) - 1}, \tag{5.68}$$

$$\beta_n = 0.125 \exp\left(\frac{-V - 65}{80}\right), \tag{5.69}$$

and

$$\bar{g}_{\text{Na}} = 120, \quad \bar{g}_{\text{K}} = 36, \quad \bar{g}_{\text{L}} = 0.3, \tag{5.70}$$

$$V_{Na} = 55, \quad V_K = -77, \quad V_L = -54.4, \quad V_{\text{eq}} = -65. \tag{5.71}$$

9. Solve the full Hodgkin–Huxley equations numerically with a variety of constant current inputs. For what range of inputs are there self-sustained oscillations? Construct the bifurcation diagram as in Exercise 6.

10. The Hodgkin–Huxley equations are for the squid axon at 6.3°C. Using that the absolute temperature enters the equations through the Nernst equation, determine how changes in temperature affect the behavior of the equations. In particular, simulate the equations at 0°C and 30°C to determine whether the equations become more or less excitable with an increase in temperature.

11. Show that a Hopf bifurcation occurs in the generalized FitzHugh–Nagumo equations when $f_v(v^*, w^*) = -\epsilon g_w(v^*, w^*)$, assuming that

$$f_v(v^*, w^*)g_w(v^*, w^*) - g_v(v^*, w^*)f_w(v^*, w^*) > 0.$$

On which side of the minimum of the v nullcline can this condition be satisfied?

12. Morris and Lecar (1981) proposed the following two-variable model of membrane potential for a barnacle muscle fiber:

$$C_m \frac{dV}{dT} + I_{\text{ion}}(V, W) = I_{\text{app}}, \tag{5.72}$$

$$\frac{dW}{dT} = \phi\Lambda(V)[W_\infty(V) - W], \tag{5.73}$$

where V = membrane potential, W = fraction of open K^+ channels, T = time, C_m = membrane capacitance, I_{app} = externally applied current, ϕ = maximum rate for closing K^+ channels, and

$$I_{\text{ion}}(V, W) = g_{\text{Ca}}M_\infty(V)(V - V_{\text{Ca}}) + g_{\text{K}}W(V - V_{\text{K}}) + g_{\text{L}}(V - V_{\text{L}}), \tag{5.74}$$

$$M_\infty(V) = \frac{1}{2}\left(1 + \tanh\left(\frac{V - V_1}{V_2}\right)\right), \tag{5.75}$$

$$W_\infty(V) = \frac{1}{2}\left(1 + \tanh\left(\frac{V - V_3}{V_4}\right)\right), \tag{5.76}$$

$$\Lambda(V) = \cosh\left(\frac{V - V_3}{2V_4}\right). \tag{5.77}$$

Typical rate constants in these equations are shown in Table 5.1.

Table 5.1 Typical parameter values for the Morris–Lecar model.

$C_m = 20\ \mu\text{F/cm}^2$	$I_{\text{app}} = 0.06\ \text{mA/cm}^2$
$g_{\text{Ca}} = 4.4\ \text{mS/cm}^2$	$g_{\text{K}} = 8\ \text{mS/cm}^2$
$g_{\text{L}} = 2\ \text{mS/cm}^2$	$\phi = 0.04\ (\text{ms})^{-1}$
$V_1 = -1.2\ \text{mV}$	$V_2 = 18\ \text{mV}$
$V_3 = 2$	$V_4 = 30\ \text{mV}$
$V_{\text{Ca}} = 120\ \text{mV}$	$V_{\text{K}} = -84\ \text{mV}$
$V_{\text{L}} = -60\ \text{mV}$	

(a) Make a phase portrait for the Morris–Lecar equations. Plot the nullclines and show some typical trajectories, demonstrating that the model is excitable.

(b) Does the Morris–Lecar model exhibit anode break excitation (see Exercise 7)? If not, why not?

13. The Pushchino model is a piecewise-linear model of FitzHugh–Nagumo type proposed as a model of the ventricular action potential. The model has

$$f(v,w) = F(v) - w, \tag{5.78}$$

$$g(v,w) = \frac{1}{\tau(v)}(v-w), \tag{5.79}$$

where

$$F(v) = \begin{cases} -30v, & \text{for} \quad v < v_1, \\ \gamma v - 0.12, & \text{for} \quad v_1 < v < v_2, \\ -30(v-1), & \text{for} \quad v > v_2, \end{cases} \tag{5.80}$$

$$\tau(v) = \begin{cases} 2, & \text{for} \quad v < v_1, \\ 16.6, & \text{for} \quad v > v_1, \end{cases} \tag{5.81}$$

with $v_1 = 0.12/(30+\gamma)$ and $v_2 = 30.12/(30+\gamma)$.

Simulate the action potential for this model. What is the effect on the action potential of changing $\tau(v)$?

14. Perhaps the most important example of a nonphysiological excitable system is the Belousov–Zhabotinsky reaction. This reaction denotes the oxidation of malonic acid by bromate in acidic solution in the presence of a transition metal ion catalyst. Kinetic equations describing this reaction are (Tyson and Fife, 1980)

$$\epsilon \frac{du}{dt} = -fv\frac{u-q}{u+q} + u - u^2, \tag{5.82}$$

$$\frac{dv}{dt} = u - v, \tag{5.83}$$

where u denotes the concentration of bromous acid and v denotes the concentration of the oxidized catalyst metal. Typical values for parameters are $\epsilon \approx 0.01, f = 1, q \approx 10^{-4}$. Describe the phase portrait for this system of equations.

15. It is not particularly difficult to build an electrical analogue of the FitzHugh–Nagumo equations with inexpensive and easily obtained electronic components. The parts list for one "cell" (shown in Fig. 5.20) includes two op-amps (operational amplifiers), two power supplies, a few resistors, and two capacitors, all readily available from any consumer electronics store (Keener, 1983).

The key component is an operational amplifier (Fig. 5.18). An op-amp is denoted in a circuit diagram by a triangle with two inputs on the left and a single output from the vertex on the right. Only three circuit connections are shown on a diagram, but two more

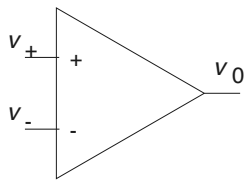

Figure 5.18 Diagram for an operational amplifier (op-amp).

are assumed, being necessary to connect with the power supply to operate the op-amp. Corresponding to the supply voltages V_{s-} and V_{s+}, there are voltages V_{r-} and V_{r+}, called the *rail voltages*, which determine the operational range for the output of an op-amp. The job of an op-amp is to compare the two input voltages v_+ and v_-, and if $v_+ > v_-$, to set (if possible) the output voltage v_0 to the high rail voltage V_{r+}, whereas if $v_+ < v_-$, then v_0 is set to V_{r-}. With reliable electronic components it is a good first approximation to assume that the input draws no current, while the output v_0 can supply whatever current is necessary to maintain the required voltage level.

The response of an op-amp to changes in input is not instantaneous, but is described reasonably well by the differential equation

$$\epsilon_s \frac{dv_0}{dt} = g(v_+ - v_-) - v_0. \tag{5.84}$$

The function $g(v)$ is continuous, but quite close to the piecewise-constant function

$$g(v) = V_{r+}H(v) + V_{r-}H(-v), \tag{5.85}$$

with $H(v)$ the Heaviside function. The number ϵ_s is small, and is the inverse of the *slew-rate*, which is typically on the order of 10^6–10^7 V/sec. For all of the following circuit analysis, take $\epsilon_s \to 0$.

(a) Show that the simple circuit shown in Fig. 5.19 is a linear amplifier, with

$$v_0 = \frac{R_1 + R_2}{R_2} v_+, \tag{5.86}$$

provided that v_0 is within the range of the rail voltages.

(b) Show that if $R_1 = 0, R_2 = \infty$, then the device in Fig. 5.19 becomes a *voltage follower* with $v_0 = v_+$.

(c) Find the governing equations for the circuit in Fig. 5.20, assuming that the rail voltages for op-amp 2 are well within the range of the rail voltages for op-amp 1.
Show that

$$C_1 \frac{dv}{dt} + i_2 \left(1 - \frac{R_4}{R_5}\right) + \frac{F(v)}{R_3} + \frac{v - v_g}{R_5} = 0, \tag{5.87}$$

$$C_2 R_5 \frac{di_2}{dt} + R_4 i_2 = v - v_g, \tag{5.88}$$

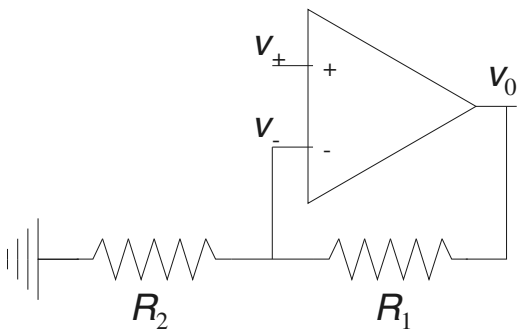

Figure 5.19 Linear amplifier using an op-amp.

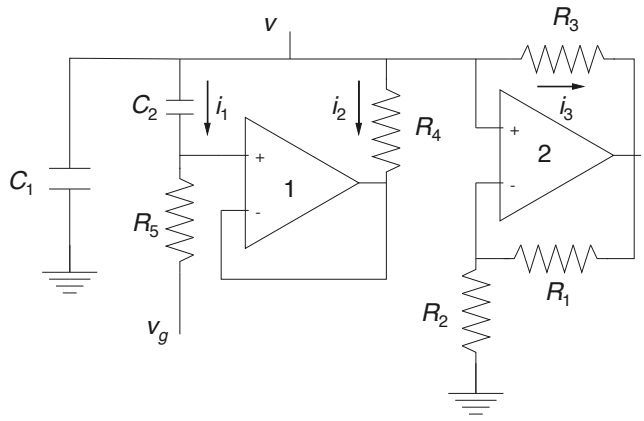

Figure 5.20 FitzHugh–Nagumo circuit using op-amps.

Table 5.2 Parts list for the FitzHugh–Nagumo analog circuit.

2 LM 741 op-amps (National Semiconductor)	
$R_1 = R_2 = 100\text{k}\Omega$	$R_3 = 2.4\Omega$
$R_4 = 1\text{k}\Omega$	$R_5 = 10\text{k}\Omega$
$C_1 = 0.01\mu\text{F}$	$C_2 = 0.5\mu\text{F}$
Power supplies:	
± 15V for op-amp #1	± 12V for op-amp #2

where $F(v)$ is the piecewise-linear function

$$F(v) = \begin{cases} v - V_{r_+}, & \text{for} \quad v > \alpha V_{r_+}, \\ -\frac{R_1}{R_2} v, & \text{for} \quad \alpha V_{r_-} \le v \le \alpha V_{r_+}, \\ v - V_{r_-}, & \text{for} \quad v < \alpha V_{r_-}, \end{cases} \tag{5.89}$$

and $\alpha = \frac{R_2}{R_1 + R_2}$.

(d) Sketch the phase portrait for these circuit equations. Show that this is a piecewise-linear FitzHugh–Nagumo system.

(e) Use the singular perturbation approximation (5.59) to estimate the period of oscillation for the piecewise-linear analog FitzHugh–Nagumo circuit in Fig. 5.20.

CHAPTER 9

Neuroendocrine Cells

There are many hormones that circulate through the body, controlling a diverse array of functions, from appetite to body temperature to blood pH. These hormones are secreted from specialized cells in various glands, such as the hypothalamus and pituitary, the pancreas, or the thyroid. Models of hormone physiology at the level of the entire body are discussed in Chapter 16. Here, we consider models of the cells that secrete the hormones, the *neuroendocrine* cells. They are called neuroendocrine (or sometimes neurosecretory) as they have many of the hallmarks of neurons, such as membrane excitability, but are specialized, not to secrete neurotransmitter into a synaptic cleft, but to secrete hormones into the blood. However, not only is there a fine line between hormones and neurotransmitters, there is also little qualitative difference between secretion into a synaptic cleft, and secretion into the bloodstream. Thus it does not pay to draw too rigid a distinction between neurons and neuroendocrine cells.

Although, unsurprisingly, there is a great variety of neuroendocrine cells, they have certain characteristics that serve to unify their study. First, they are excitable and therefore have action potentials. Second, the electrical activity usually is not a simple action potential, or periodic train of action potentials (Chapter 5). Instead, the action potentials are characterized by bursts of rapid oscillatory activity interspersed with quiescent periods during which the membrane potential changes only slowly. This behavior is called *bursting*. Third, bursting is often closely regulated by the intracellular Ca^{2+} concentration (Chapter 7). Thus, models of neurosecretory cells typically combine models of membrane electrical excitability and Ca^{2+} excitability, leading to a fascinating array of dynamic behaviors.

Other factors can also influence bursting; for example, as is described later in this chapter, recent models of bursting in the pancreatic β cell include models of the glycolytic pathway, thus leading to models that incorporate, in a single cell, many of the

complexities described in Chapters 1, 5 and 7. Neuroendocrine cells are thus wonderful examples of how multiple oscillatory mechanisms can interact, and provide an enormous range of interesting behaviors to explore.

9.1 Pancreatic β Cells

In response to glucose, β cells of the pancreatic islet secrete insulin, which causes the increased use or uptake of glucose in target tissues such as muscle, liver, and adipose tissue. When blood levels of glucose decline, insulin secretion stops, and the tissues begin to use their energy stores instead. Interruption of this control system results in diabetes, a disease that, if left uncontrolled, can result in kidney failure, heart disease, and death. It is believed that bursting, a typical example of which is shown in Fig. 9.1, plays an important (but not exclusive) role in the release of insulin from β cells.

9.1.1 Bursting in the Pancreatic β Cell

Bursting in the pancreatic β cell occurs with a wide variety of periods, ranging from a few seconds to a few minutes. Typically, these are divided into three groups; fast bursting, with periods of around 2 to 5 s; medium bursting, with periods of around 10 to 60 s; and slow bursting, with periods of around 2 to 4 minutes.

Although bursting has been studied extensively for many years, most mathematical studies are based on the pioneering work of Rinzel (1985, 1987), which was in turn based on one of the first biophysical models of a pancreatic β cell (Chay and Keizer, 1983). Rinzel's interpretation of bursting in terms of nonlinear dynamics provides an excellent example of how mathematics can be used to understand complex biological dynamical systems.

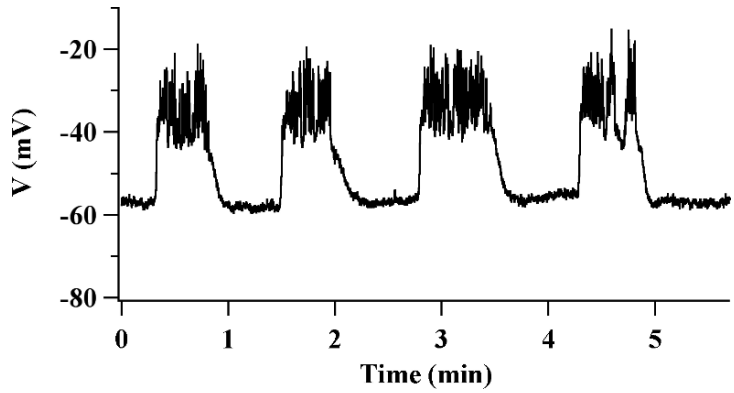

Figure 9.1 Bursting oscillations in the pancreatic β cell. Provided by Les Satin, Min Zhang and Richard Bertram.

Models of bursting in pancreatic β cells can be divided into two major groups (well summarized by de Vries, 1995). Earlier models were generally based on the assumption that bursting was caused by an underlying slow oscillation in the intracellular Ca^{2+} concentration (Chay, 1986, 1987; Chay and Cook, 1988; Chay and Kang, 1987; Himmel and Chay, 1987; Keizer and Magnus, 1989). In light of more recent experimental evidence showing that Ca^{2+} is not the slow variable underlying bursting, more recent models have modified this assumption, relying on alternative mechanisms to produce the underlying slow oscillation (Keizer and Smolen, 1991; Smolen and Keizer, 1992; Bertram and Sherman, 2004a,b; Nunemaker et al., 2006).

One of the first models of bursting was proposed by Atwater et al. (1980). It was based on extensive experimental data, incorporating the important cellular mechanisms that were thought to underlie bursting, and was later developed into a mathematical model by Chay and Keizer (1983). Although the mathematical model includes only those processes believed to be essential to the bursting process and thus omits many features of the cell, it is able to reproduce many of the basic properties of bursting. The ionic currents in the model are:

1. A Ca^{2+}-activated K^+ channel with conductance an increasing function of $c = [Ca^{2+}]$ of the form

$$g_{K,Ca} = \bar{g}_{K,Ca}\frac{c}{K_d + c}, \tag{9.1}$$

   for some constant $\bar{g}_{K,Ca}$.
2. A voltage-gated K^+ channel modeled in the same way as in the Hodgkin–Huxley equations, with

$$g_K = \bar{g}_K n^4, \tag{9.2}$$

   where n obeys the same differential equation as in the Hodgkin–Huxley equations (Chapter 5), except that the voltage is shifted by V^*, so that V in (5.28) and (5.29) is replaced by $V + V^*$. For example, $\beta_n(V) = 0.125\exp[(-V - V^*)/80]$.
3. A voltage-gated Ca^{2+} channel, with conductance

$$g_{Ca} = \bar{g}_{Ca} m^3 h, \tag{9.3}$$

   where m and h satisfy Hodgkin–Huxley differential equations for Na^+ gating, shifted along the voltage axis by V'. That is, the inward Ca^{2+} current is modeled by the Na^+ current of the Hodgkin–Huxley equations.

Combining these ionic currents and adding a leak current gives

$$C_m\frac{dV}{dt} = -(g_{K,Ca} + g_K)(V - V_K) - 2g_{Ca}(V - V_{Ca}) - g_L(V - V_L), \tag{9.4}$$

where C_m is the membrane capacitance.

To complete the model, there is an equation for the regulation of intracellular Ca^{2+},

$$\frac{dc}{dt} = f(-k_1 I_{Ca} - k_c c), \tag{9.5}$$

where the Ca^{2+} current is $I_{Ca} = \bar{g}_{Ca} m^3 h(V - V_{Ca})$ and where k_1 and k_c are constants. The constant f is a scale factor relating total changes in $[Ca^{2+}]$ to the changes in free $[Ca^{2+}]$ (as discussed in the section on Ca^{2+} buffering in Chapter 7) and is usually a small number, while k_c is the rate at which Ca^{2+} is removed from the cytoplasm by the membrane ATPase pump.

For this model it is assumed that glucose regulates the rate of removal of Ca^{2+} from the cytoplasm. Thus, k_c is assumed to be an (unspecified) increasing function of glucose concentration. However, the concentration of glucose is not a dynamic variable of the model, so that k_c can be regarded as fixed, and the behavior of the model can be studied for a range of values of k_c.

A numerically computed solution of this model, shown in Fig. 9.2, exhibits bursts that bear a qualitative resemblance to those seen experimentally. It is also readily seen that there is a slow oscillation in c underlying the bursts, with bursting occurring during the peak of the Ca^{2+} oscillation. The fact that Ca^{2+} oscillations occur on a slower time scale is built into the Ca^{2+} equation (9.5) explicitly by means of the parameter f. As f becomes smaller, the Ca^{2+} equation evolves more slowly, and thus the relative speeds of

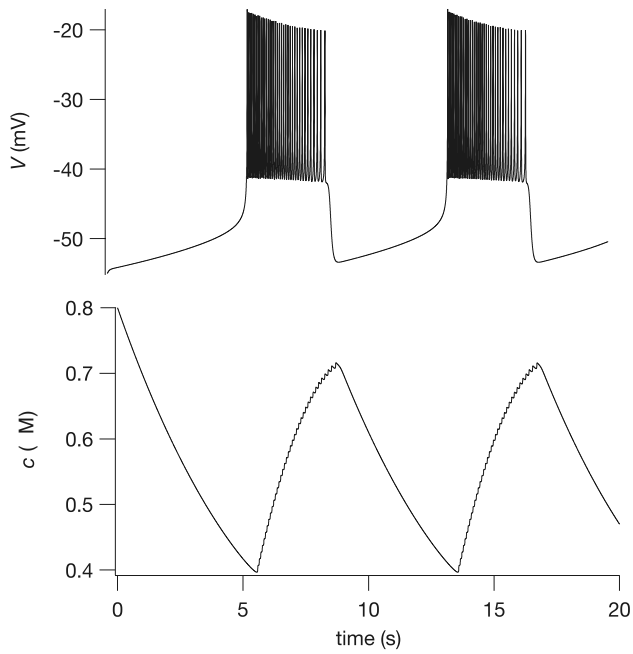

Figure 9.2 Bursting oscillations in the Chay–Keizer β cell model, calculated using the parameter values in Table 9.1.

Table 9.1 Parameters of the model of electrical bursting in pancreatic β cells.

C_m	$= 1\ \mu\text{F/cm}^2$	$\bar{g}_{\text{K,Ca}}$	$= 0.02\ \text{mS/cm}^2$
$\bar{g}_{\text{K}}$	$= 3\ \text{mS/cm}^2$	$\bar{g}_{\text{Ca}}$	$= 3.2\ \text{mS/cm}^2$
$\bar{g}_{\text{L}}$	$= 0.012\ \text{mS/cm}^2$	V_{K}	$= -75\ \text{mV}$
V_{Ca}	$= 100\ \text{mV}$	V_{L}	$= -40\ \text{mV}$
V^*	$= 30\ \text{mV}$	V'	$= 50\ \text{mV}$
K_d	$= 1\ \mu\text{M}$	f	$= 0.007$
k_1	$= 0.0275\ \mu\text{M cm}^2/\text{nC}$	k_c	$= 0.02\ \text{ms}^{-1}$

the voltage and Ca^{2+} equations are directly controlled. It therefore appears that there are two oscillatory processes interacting to give bursting, with a fast oscillation in V superimposed on a slower oscillation in c. This is the basis of the phase-plane analysis that we describe next.

Phase-Plane Analysis

The β cell model can be simplified by ignoring the dynamics of m and h, thus removing the time dependence (but not the voltage dependence) of the Ca^{2+} current (Rinzel and Lee, 1986). The simplified model equations are

$$C_m \frac{dV}{dt} = -I_{\text{Ca}}(V) - \left(\bar{g}_{\text{K}} n^4 + \frac{\bar{g}_{\text{K,Ca}} c}{K_d + c}\right)(V - V_{\text{K}}) - \bar{g}_{\text{L}}(V - V_{\text{L}}), \tag{9.6}$$

$$\tau_n(V)\frac{dn}{dt} = n_\infty(V) - n, \tag{9.7}$$

$$\frac{dc}{dt} = f(-k_1 I_{\text{Ca}}(V) - k_c c), \tag{9.8}$$

where $I_{\text{Ca}} = \bar{g}_{\text{Ca}} m_\infty^3(V) h_\infty(V)(V - V_{\text{Ca}})$.

Since f is small, this β cell model separates into a fast subsystem (the V and n equations) and a slow equation for c. The fast subsystem can be studied using phase-plane methods, and then the behavior of the full system can be understood as slow variations of the fast phase plane system.

We first consider the structure of the fast subsystem as a function of c, treating c as a fixed parameter.

When c is low, the Ca^{2+}-activated K^+ channel is not activated, and the fast subsystem has a unique fixed point with V high. Conversely, when c is high, the Ca^{2+}-activated K^+ channel is fully activated, and the fast subsystem has a unique fixed point with V low, as the high conductance of the Ca^{2+}-activated K^+ channels pulls the membrane potential closer to the K^+ Nernst potential, about -75 mV. However, for intermediate values of c there are three fixed points, and the phase plane is much more intricate.

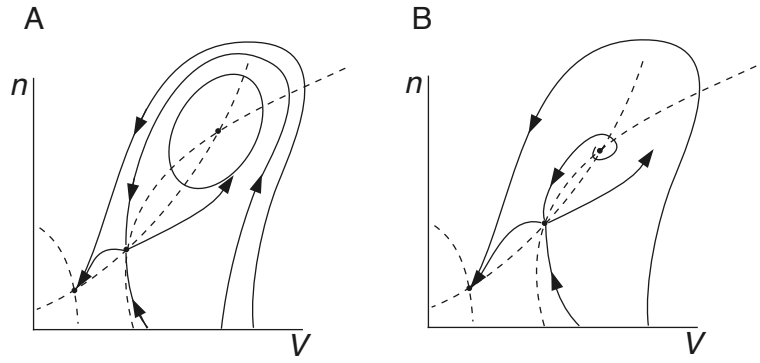

Figure 9.3 Phase planes of the fast subsystem of the Chay–Keizer β cell model, for two different values of c, both in the intermediate range. The phase planes are sketched, not drawn to scale. Nullclines are denoted by dashed lines, and the intersections of the nullclines show the positions of the fixed points. For both values of c there are three fixed points, of which the middle one is a saddle point. However, in A (with $c_{hb} < c < c_{hc}$; see Fig. 9.4) the unstable node is surrounded by a stable limit cycle, while in B (corresponding to $c > c_{hc}$) the limit cycle has disappeared via a homoclinic bifurcation.

Phase planes of the V, n subsystem for two different intermediate values of c are shown in Fig. 9.3.

In both cases, the lower fixed point is stable, the middle fixed point is a saddle point, and the upper fixed point is unstable. For some values of c the upper fixed point is surrounded by a stable limit cycle, which in turn is surrounded by the stable manifold of the saddle point (Fig. 9.3A). However, as c increases (still in the intermediate range), the limit cycle "hits" the saddle point and forms a homoclinic connection (a homoclinic bifurcation). Increasing c further breaks the homoclinic connection, and the stable manifold of the saddle point forms a heteroclinic connection with the upper, unstable, critical point (Fig. 9.3B). There is now no limit cycle.

This sequence of bifurcations can be summarized in a bifurcation diagram, with V plotted against the control parameter c (Fig. 9.4A). The Z-shaped curve is the curve of fixed points, and as usual, the stable oscillation around the upper steady state is depicted by the maximum and minimum of V through one cycle. As c increases, oscillations appear via a Hopf bifurcation (c_{hb}) and disappear again via a homoclinic bifurcation (c_{hc}). For a range of values of c the fast subsystem is bistable, with a lower stable fixed point and an upper stable periodic orbit. This bistability is crucial to the appearance of bursting.

We now couple the dynamics of the fast subsystem to the slower dynamics of c. Included in Fig. 9.4A is the curve defined by $dc/dt = 0$, i.e., the c nullcline. When V is above the c nullcline, $dc/dt > 0$, and so c increases, but when V is below the c nullcline, c decreases. Now suppose V starts on the lower fixed point for a value of c that is greater than c_{hc}. Since V is below the c nullcline, c starts to decrease, and

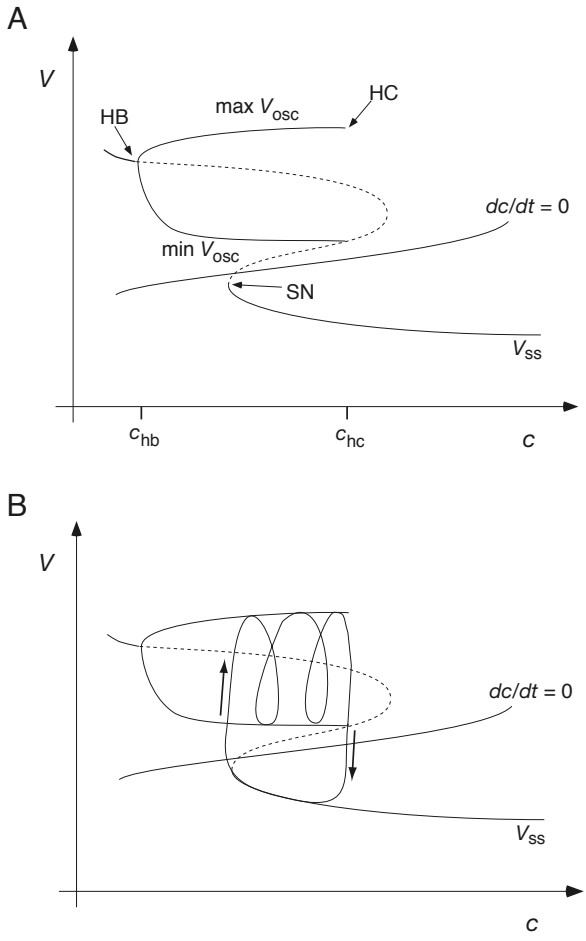

Figure 9.4 A: Sketch of the bifurcation diagram of the simplified Chay–Keizer β cell model, with c as the bifurcation parameter. V_{ss} denotes the curve of steady states of V as a function of c. A solid line indicates a stable steady state; a dashed line indicates an unstable steady state. The two branches of V_{osc} denote the maximum and minimum of V over one oscillatory cycle. HB denotes a Hopf bifurcation, HC denotes a homoclinic bifurcation, and SN denotes a saddle-node bifurcation. B: A burst cycle projected on the (V, c) plane. (Adapted from Rinzel and Lee, 1986, Fig. 3.)

V follows the lower branch of fixed points. However, when c becomes too small, this lower branch of fixed points disappears in a saddle-node bifurcation (SN), and so V must switch to the upper branch of the Z-shaped curve. Since this upper branch is unstable and surrounded by a stable limit cycle, V begins to oscillate. However, since V now lies entirely above the c nullcline, c begins to increase. Eventually, c increases enough to cross the homoclinic bifurcation at c_{hc}, the stable limit cycles disappear, and V switches back to the lower branch, completing the cycle. Repetition of this process causes bursting. The quiescent phase of the bursting cycle is when V is on the lower branch of the Z-shaped curve, and during this phase V increases slowly. A burst of oscillations occurs when V switches to the upper branch, and disappears again after passage through the homoclinic bifurcation. Clearly, in this scenario, bursting relies on the coexistence of both a stable fixed point and a stable limit cycle, and the bursting cycle is a hysteresis loop that switches between branches of the Z-shaped curve. Bursting also relies on the c nullcline intersecting the Z-shaped curve in the

right location. For example, if the c nullcline intersects the Z-shaped curve on its lower branch, there is a unique stable fixed point for the whole system, and bursting does not occur. A projection of the bursting cycle on the (V, c) phase plane is shown in Fig. 9.4B. The periods of the oscillations in the burst increase through the burst, as the limit cycles get closer to the homoclinic trajectory, which has infinite period.

The relationship between bursting patterns and glucose concentration can also be deduced from Fig. 9.4. Notice that the $\frac{dc}{dt} = 0$ nullcline, given by $c = -\frac{k_1}{k_c} I_{\mathrm{Ca}}(V)$, is inversely proportional to k_c. Increasing k_c moves the $\frac{dc}{dt} = 0$ nullcline to the left while decreasing k_c moves it to the right. Thus, when k_c is sufficiently small, the nullcline intersects the lower branch of the V nullcline. On the other hand, if k_c is extremely large, the c nullcline intersects the upper branch of the V nullcline, possibly to the left of c_{hb}. At intermediate values of c, the c nullclines intersects the middle branch of the V nullcline.

Under the assumption that k_c is monotonically related to the glucose concentration, when the glucose concentration is low, the system is at a stable rest point on the lower V nullcline; there is no bursting. If glucose is increased so that the c nullcline intersects the middle V nullcline with $c < c_{\mathrm{hc}}$, there is bursting. However, the length of the bursting phase increases and the length of the resting phase decreases with increasing glucose, because Ca^{2+} increases at a slower rate and decreases at a faster rate when k_c is increased. For large enough k_c the bursting is sustained with no rest phase, as c becomes stalled below c_{hc}. Finally, at extremely high k_c values, bursting is replaced by a permanent high membrane potential, with $c < c_{\mathrm{hb}}$. This dependence of the bursting phase on glucose is confirmed by experiments.

9.1.2 ER Calcium as a Slow Controlling Variable

There are two major problems with the above model. First, it does not reproduce the wide variety of periods and bursting patterns actually seen in bursting pancreatic β cells, being limited to a narrow range of fast bursting frequencies.

Second, more recent experimental evidence has shown that Ca^{2+} oscillates much too fast to be viewed as a slow control variable. This is illustrated in Fig. 9.5, which shows simultaneous Ca^{2+} and voltage measurements. The bursting oscillations in the voltage are mirrored by bursting oscillations in the cytoplasmic Ca^{2+} concentration, and the rise in Ca^{2+} concentration is almost as fast as the rise in voltage.

So the question arises of what controls the length of bursting. One possibility is that the ER Ca^{2+} concentration varies much more slowly than the cytoplasmic Ca^{2+} and could provide the necessary control mechanism. This would be the case if most of the Ca^{2+} during active bursting were coming from the extracellular space through transmembrane ion channels, and only a small amount of Ca^{2+} flowed between the cytoplasm and the ER. If this were the case, ER Ca^{2+} would act like a low pass filter for cytoplasmic Ca^{2+}, and therefore could be used to detect and regulate the length of bursting activity. The possible usefulness of a low-pass filter is seen in the Ca^{2+} traces shown in Fig. 9.5, where, during a burst, Ca^{2+} concentration oscillates rapidly around

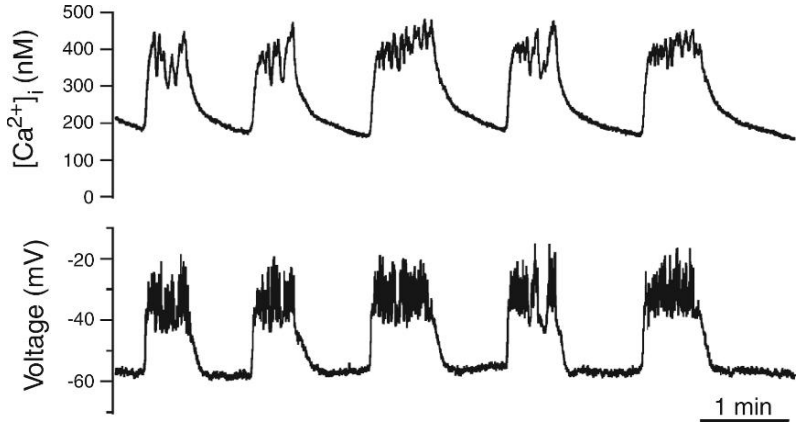

Figure 9.5 Simultaneous Ca^{2+} and voltage measurements from a bursting pancreatic β cell. (Adapted from Zhang et al., 2003, Fig. 4.)

a raised baseline. A low-pass filter would measure the length of time that the Ca^{2+} baseline is elevated, but filter out the rapid oscillations.

Thus, it was proposed by Chay (1996a,b, 1997) that slow variations in ER Ca^{2+} could be an important control mechanism, and could, in addition, generate a wider range of bursting periods. This proposal was analyzed in detail by Bertram and Sherman (2004a) who showed that the interaction of a (not very slow) cytoplasmic Ca^{2+} variable, with a (much slower) ER Ca^{2+} variable, could lead to bursting with a wide range of periods. They named this a *phantom bursting* model, as it can lead to bursting with a period intermediate between that of the slow variables.

The Membrane Voltage Submodel

The electrical part of the phantom bursting model is similar to the Chay–Keizer model, but with slight differences, so we present it in full here. As before, the current is the sum of a Ca^{2+} current, a K^+ current, and a Ca^{2+}-sensitive K^+ current, with an additional ATP-sensitive K^+ current, which is important below. The only current not assumed to be at pseudo-steady state is the K^+ current. Thus,

$$C_m \frac{dV}{dt} = -I_{\mathrm{Ca}} - I_{\mathrm{K}} - I_{\mathrm{K,Ca}} - I_{\mathrm{K,ATP}}, \tag{9.9}$$

$$\tau_n \frac{dn}{dt} = n_\infty(V) - n, \tag{9.10}$$

$$I_{\mathrm{Ca}} = g_{\mathrm{Ca}} m_\infty(V)(V - V_{\mathrm{Ca}}), \tag{9.11}$$

$$I_{\mathrm{K}} = g_{\mathrm{K}} n (V - V_{\mathrm{K}}), \tag{9.12}$$

$$I_{\mathrm{K,Ca}} = g_{\mathrm{K,Ca}} \omega(c)(V - V_{\mathrm{K}}), \tag{9.13}$$

$$I_{\mathrm{K,ATP}} = g_{\mathrm{K,ATP}}(V - V_{\mathrm{K}}), \tag{9.14}$$

where c denotes the free cytoplasmic Ca^{2+} concentration. The functions m_∞ and n_∞ are given by

$$m_\infty(V) = \frac{1}{1 + e^{(v_m - V)/s_m)}}, \tag{9.15}$$

$$n_\infty(V) = \frac{1}{1 + e^{(v_n - V)/s_n)}}. \tag{9.16}$$

The variable ω is the fraction of open Ca^{2+}-sensitive K^+ channels, and is close to a step function,

$$\omega(c) = \frac{c^5}{c^5 + k_D^5}. \tag{9.17}$$

The Calcium Submodel

These equations for the electrical properties of the membrane must be coupled to equations that model the cytoplasmic and ER Ca^{2+} concentrations. The Ca^{2+} model is chosen to be relatively simple; more complex models of Ca^{2+} dynamics are discussed in Chapter 7.

As usual, let c and c_e denote the free concentrations of Ca^{2+} in the cytoplasm and ER respectively. The equations for c and c_e are simple balances of fluxes.

1. I_{Ca}, the transmembrane Ca^{2+} current as discussed above.
2. Pumping of Ca^{2+} across the plasma and ER membranes, denoted by J_{pm} and J_{serca} respectively. Both of these fluxes are assumed to be linear functions of Ca^{2+}, and thus

$$J_{serca} = k_{serca} c, \tag{9.18}$$

$$J_{pm} = k_{pm} c. \tag{9.19}$$

3. J_{leak}, a leak from the ER. This is assumed to be proportional to the difference between the ER and cytoplasmic concentrations, and thus

$$J_{leak} = k_{leak}(c_e - c). \tag{9.20}$$

Because of Ca^{2+} buffering, only a small fraction of each flux contributes to a change in the free Ca^{2+} concentration. If we assume that buffering is fast and unsaturated, then we need only multiply each flux by a scaling factor to get the change in free Ca^{2+} concentration (Section 7.4).

We put all these fluxes together to get

$$\frac{dc}{dt} = f_{cyt}(-\alpha I_{Ca} - J_{pm} + J_{leak} - J_{serca}), \tag{9.21}$$

$$\frac{dc_e}{dt} = -\gamma f_{er}(J_{leak} - J_{serca}). \tag{9.22}$$

Here, γ is the ratio of the cytoplasmic volume to the ER volume, while f_{cyt} and f_{er} are the buffering scaling factors for the cytoplasm and the ER.

Table 9.2 Parameters of the phantom bursting model. The values of $g_{K,Ca}$ and $g_{K,ATP}$ used for each simulation are given in the figure captions.

g_{Ca}	$= 1200$ pS	g_K	$= 3000$ pS
V_{Ca}	$= 25$ mV	V_K	$= -75$ mV
C_m	$= 5300$ fF	α	$= 4.5 \times 10^{-6} \mu$M fA^{-1} ms^{-1}
τ_n	$= 16$ ms	f_{cyt}	$= 0.01$
k_{pm}	$= 0.2$ ms^{-1}	k_D	$= 0.3\ \mu$M
v_n	$= -16$ mV	s_n	$= 5$ mV
v_m	$= -20$ mV	s_m	$= 12$ mV
k_{serca}	$= 0.4$ ms^{-1}	f_{er}	$= 0.01$
γ	$= 5$	p_{leak}	$= 0.0005$ ms^{-1}

The parameter values for this model are given in Table 9.2.

Fast Bursting

When the Ca^{2+}-sensitive K^+ conductance is high (900 pS), the model exhibits fast bursting, as shown in Fig. 9.6. The ER Ca^{2+} concentration varies little over the course of a burst, and indeed, if c_e is set to be a constant, the solution is nearly identical. As can be seen from the middle panel of Fig. 9.6, although c is slightly slower than V, it changes a lot faster than c_e, and is not obviously a slow variable.

A full analysis of this model requires examining a three-dimensional phase space, a difficult exercise. However, even though it is only an approximate analysis, it is useful to analyze this model in the same way as Rinzel's analysis of the Chay–Keizer model, as discussed previously. To do so, we pretend that c is a bifurcation parameter, and draw the bifurcation diagram of V against c (Fig. 9.7). This gives a diagram qualitatively similar to that shown in Fig. 9.4. A Z-shaped curve of steady-state solutions becomes unstable at a Hopf bifurcation, and the branch of stable limit cycles intersects the Z-shaped curve of steady states in a homoclinic bifurcation. This gives rise to bistability, where a stable steady state and a stable limit cycle exist simultaneously.

Bursting occurs in the same manner as the Chay–Keizer model. Above the $dc/dt = 0$ nullcline the solution trajectory moves to the right, and lives (approximately) on the branch of stable limit cycles, giving the active phase of the burst. When it moves far enough to the right, it falls off the branch of limit cycles and heads to the lower branch of stable steady states. Since this branch is below the c nullcline, the solution then moves to the left, eventually falling off the saddle-node to repeat the cycle. This way of interpreting the solution is only an approximate one, as it can be seen from Fig. 9.7 that the actual solution follows accurately neither the branch of periodic orbits nor

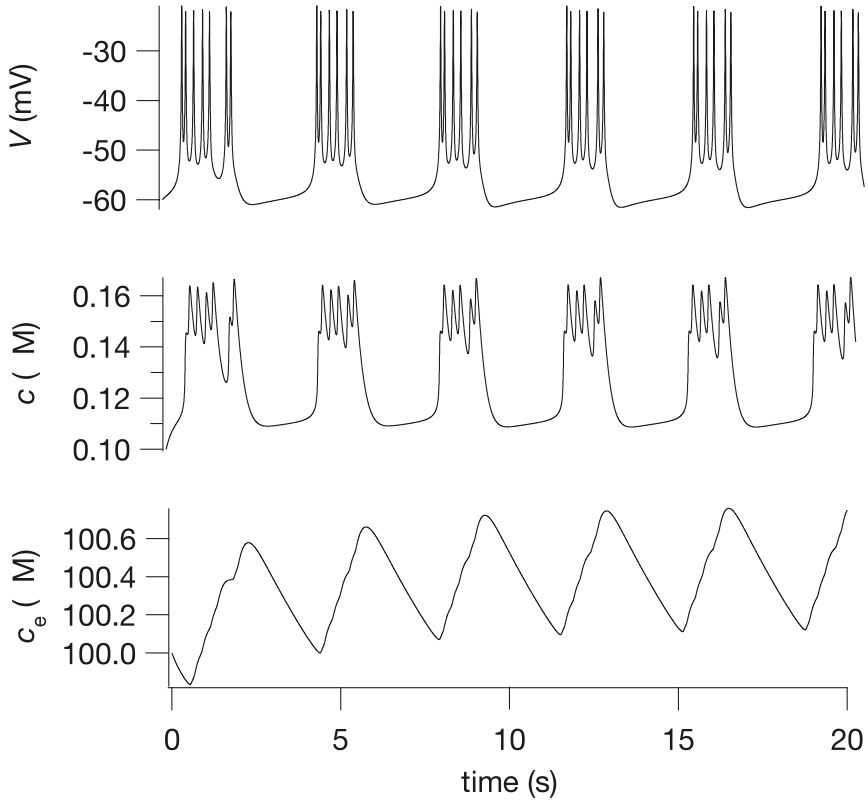

Figure 9.6 Fast bursting oscillations in the phantom bursting model. These solutions were computed with $g_{K,Ca} = 900$ pS and $g_{K,ATP} = 227.5$ pS. Note that the ER Ca^{2+} varies only slightly.

the lower branch of steady states. The upper turning point of the burst is close to $\text{osc}_{\max}$, but the lower turning point is not close at all to $\text{osc}_{\min}$. Similarly, when the solution falls off the branch of periodic orbits, it does so well before the homoclinic bifurcation, and then does not follow the lower branch of steady states closely. This happens because c is not really a slow parameter after all. In the limit as c becomes infinitely slow, the solution would track much more closely the bifurcation diagram of the fast subsystem. Despite these quantitative disagreements, the phase plane of the fast subsystem is nonetheless a useful way to interpret and understand the solutions of the full system.

However, there is one important difference between this model and the Chay–Keizer model. In this model there is a second slow variable, c_e, and thus the $dc/dt = 0$ nullcline moves as c_e varies (the Z-shaped curve, however, is independent of c_e). From (9.21) we see that the $dc/dt = 0$ nullcline is given by

$$c = \frac{p_{\text{leak}} c_e - \alpha I_{\text{Ca}}}{k_{\text{pm}} + p_{\text{leak}} + k_{\text{serca}}}, \tag{9.23}$$

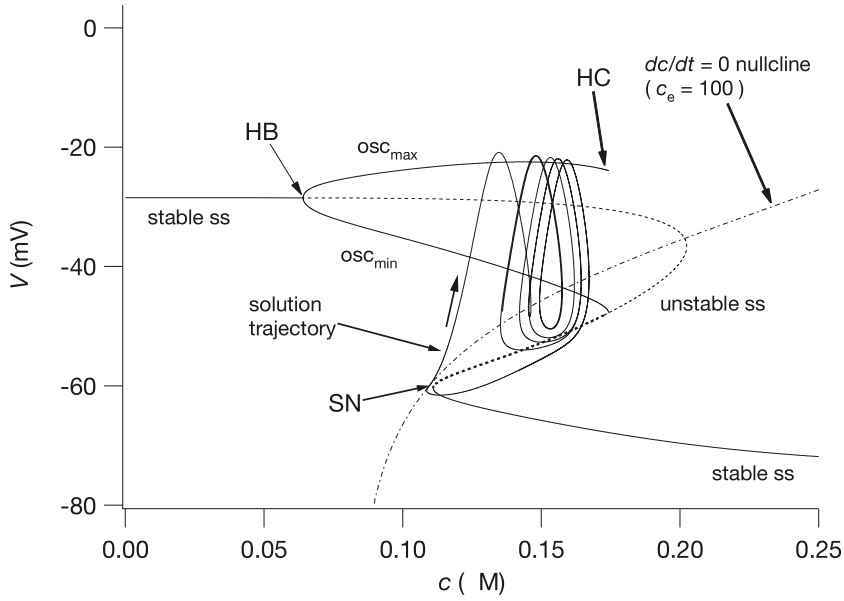

Figure 9.7 Fast bursting in the phantom bursting model (computed with $g_{K,Ca} = 900$ pS and $g_{K,ATP} = 227.5$ pS) superimposed on the bifurcation diagram of the fast subsystem, treating c as the bifurcation parameter. HB — Hopf bifurcation; HC — homoclinic bifurcation; SN — saddle-node bifurcation.

and thus, as c_e increases, the nullcline moves to the right. For the fast bursting shown in Fig. 9.6 the changes in c_e are so small that this movement of the nullcline has no effect on the bursting. However, for different parameter values, more interesting behaviors emerge.

Medium Bursting

One way to get a longer burst period would be to stretch the Z-shaped curve horizontally, so that the homoclinic bifurcation and the saddle-node are further apart. This can be accomplished by decreasing $g_{K,Ca}$. However, if the c nullcline remains unchanged, for small enough $g_{K,Ca}$ it intersects the Z-shaped curve on its upper branch, inside the branch of stable limit cycles. In this case, the limit cycle is a stable solution of the full system, and the solution remains stuck in the active phase.

Now the slow dynamics of c_e come into play. During the active phase c_e increases (see Exercise 4), gradually moving the c nullcline to the right; the oscillations chase the c nullcline to the right, as shown in Fig. 9.8. When the c nullcline is moved far enough to the right, the solution falls off the limit cycles (i.e., leaves the active phase), moves toward the lower branch of steady-state solutions (thus starting the silent phase), and moves to the left toward the saddle-node. However, movement along this lower branch is very slow, as the c nullcline intersects the Z-shaped curve on its lower branch, giving

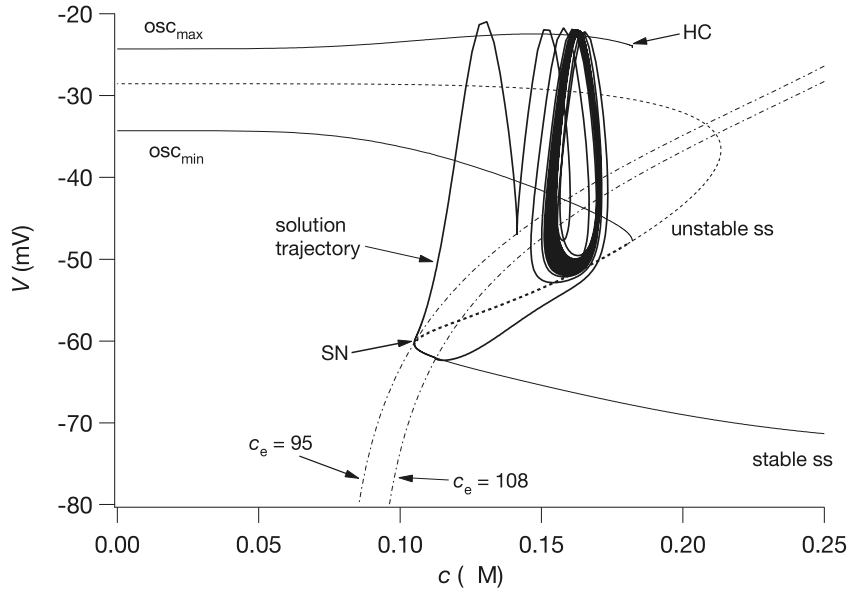

Figure 9.8 Medium bursting in the phantom bursting model (computed with $g_{K,Ca} = 700$ pS and $g_{K,ATP} = 300$ pS) superimposed on the bifurcation diagram of the fast subsystem, treating c as the bifurcation parameter. HC — homoclinic bifurcation; SN — saddle-node bifurcation. The Hopf bifurcation occurs at a negative value of c and so does not appear here.Two $dc/dt = 0$ nullclines are shown, for the maximum and minimum values of c_e over a burst.

a stable quasi-steady state. The solution is thus forced to move at the same speed as the slow variable c_e, tracking the quasi-steady state as it moves to the left. Eventually, the c nullcline moves sufficiently far to the left that the quasi-steady state disappears, the solution leaves the lower branch of the Z-shaped curve, and the burst cycle repeats.

Thus, in medium bursting the burst cycle relies on the slow movement of the c nullcline, which is caused by the slow increase of c_e during the active phase of the burst, and the slow decrease of c_e during the silent phase. Because the c nullcline moves slowly, this results in medium bursting with a longer period. Both the active and silent phases are longer than for fast bursting, giving a much longer burst period, and the ER Ca^{2+} varies much more over a cycle. Typical solutions are shown in Fig. 9.9.

The Effect of Agonists

Pancreatic β cells are also regulated by the nervous system. Secretion of acetylcholine from parasympathetic nerves increases the rate of insulin secretion, an effect due partly to changes in the electrical activity and Ca^{2+} dynamics of individual β cells. Since the action of acetylcholine is via the production of inositol trisphosphate (IP_3; see Chapter 7), and consequent release of Ca^{2+} from the ER, it can be modeled by including an additional term for a Ca^{2+} flux through IP_3 receptors (Exercise 3). When $[IP_3]$ is raised

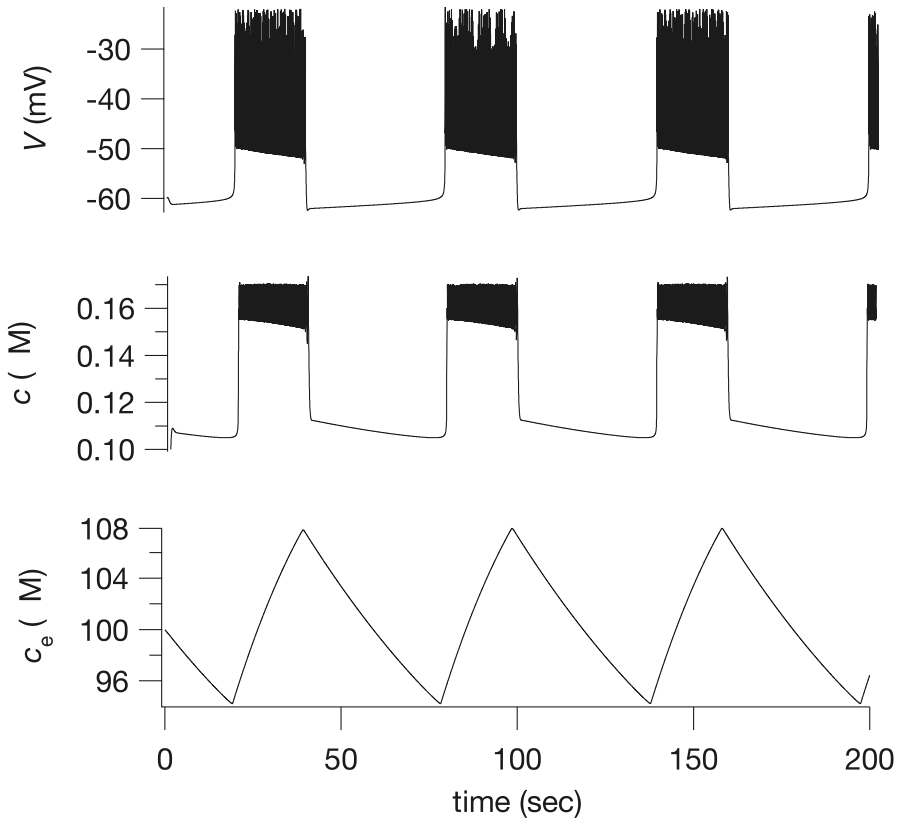

Figure 9.9 Medium bursting oscillations in the phantom bursting model. These solutions were computed with $g_{K,Ca} = 700$ pS and $g_{K,ATP} = 300$ pS. The active phase is not completely regular due to inadequate numerical resolution of the timestep.

from 0 to 0.3 μM the burst pattern changes from medium to fast, a change which is observed experimentally.

9.1.3 Slow Bursting and Glycolysis

Bursting in pancreatic β cells is highly sensitive to the level of glucose; as the concentration of glucose increases, so does the active fraction of the burst cycle. During the active fraction of the burst cycle the Ca^{2+} concentration is raised, and this in turn causes the secretion of insulin. Thus, the rate of insulin secretion is an increasing function of glucose concentration.

This effect of glucose is believed to be mediated by the ATP-sensitive K^+ channel, which is activated by ADP and inhibited by ATP. At low glucose concentrations the ATP/ADP ratio is low, the K^+ channel is open, hyperpolarizing the cell and thus preventing bursting. As glucose increases, so does the ATP/ADP ratio; this decreases the

conductance of the ATP-sensitive K^+ channels, thus depolarizing the cell and allowing bursting to occur.

There are two important features of bursting and insulin secretion that we have not, as yet, addressed. First, bursting often occurs with a much longer period than that so far reproduced by the models above, and second, such slow bursting can take a more complex form than that shown in Figs. 9.6 and 9.9. In particular, slow bursting can occur as "compound" bursting, or bursts of bursts, in which each active phase itself consists of alternating active and silent subphases.

One hypothesis is that compound bursting and a long burst period arise from a slow oscillation in the glycolytic pathway (Chapter 1), which causes slow oscillations in the ATP/ADP ratio. One of the earliest quantitative models of this hypothesis was that of Wierschem and Bertram (2004), who showed that, by linking the Goldbeter–Lefever model of glycolytic oscillations (Chapter 1) to a simple bursting model, the burst pattern could be modulated on a long time scale, to obtain both compound and slow bursting. This initial model, more a proof of principle than a quantitative model, was quickly followed by much more detailed realizations, first using the Smolen model of glycolytic oscillations (Smolen, 1995; Bertram et al., 2004; Nunemaker et al., 2006), and then linking the Smolen model to the Magnus–Keizer model of mitochondrial metabolism (Magnus and Keizer, 1997, 1998a, 1998b; Bertram et al., 2006a, 2007a,b).

The later models being too complex to present in full here, we instead examine briefly the original model of Wierschem and Bertram (2004), as it contains most of the essentials of the more complex models.

The Glycolysis, Electrical and Calcium Submodels

To model glycolytic oscillations in a simple way we use the reduced Goldbeter–Lefever model discussed in Section 1.6. Thus,

$$\tau_c \frac{d[\mathrm{ATP}]}{dt} = v_1 - F([\mathrm{ATP}], [\mathrm{ADP}]), \tag{9.24}$$

$$\tau_c \frac{d[\mathrm{ADP}]}{dt} = F([\mathrm{ATP}], [\mathrm{ADP}]) - v_2[\mathrm{ADP}], \tag{9.25}$$

where (as in (1.125))

$$F([\mathrm{ATP}], [\mathrm{ADP}]) = [\mathrm{ATP}](1 + k_{\mathrm{ADP}}[\mathrm{ADP}])^2. \tag{9.26}$$

The only change introduced to this version of the glycolytic model is the time constant, τ_c, which is convenient for changing the period of the glycolytic oscillations.

The electrical submodel is almost the same as the models discussed previously in this chapter. The currents are described by (9.9)–(9.14) and (9.15), the only difference being that, instead of (9.17), we take

$$\omega(c) = \frac{c}{c + k_D}. \tag{9.27}$$

Table 9.3 Parameters of the compound bursting model.

g_{Ca}	$= 1200$ pS	g_K	$= 3000$ pS
$g_{K,Ca}$	$= 300$ pS	$g_{K,ATP}$	$= 350$ pS
V_{Ca}	$= 25$ mV	V_K	$= -75$ mV
C_m	$= 5300$ fF	α	$= 2.25 \times 10^{-6} \mu$M fA^{-1} ms^{-1}
τ_n	$= 16$ ms	f	$= 0.001$
k_c	$= 0.1$ ms^{-1}	k_D	$= 0.3\ \mu$M
v_n	$= -16$ mV	s_n	$= 5.6$ mV
v_m	$= -20$ mV	s_m	$= 12$ mV
τ_c	$= 1.2 \times 10^{-6}$ ms	v_1	$= 10$ mM
v_2	$= 185$	k_{ADP}	$= 20$ mM^{-1}

Finally, the Ca^{2+} submodel is the same as that of the Chay–Keizer model. We thus ignore ER Ca^{2+} to get a single equation for c (as in (9.5)),

$$\frac{dc}{dt} = -f(\alpha I_{Ca} + k_c c). \tag{9.28}$$

All the parameters of the compound bursting model are given in Table 9.3.

Compound Bursting

A typical example of compound bursting in this model is shown in Fig. 9.10. The bursting occurs in clusters, with the duration of the active phase increasing and then decreasing through each cluster. As can be seen from the dotted curve, [ATP] is oscillating also; here these oscillations are independent of c and V, although this is not necessarily so in more complex models.

The reason for the compound bursting can be seen if we consider the fast–slow bifurcation structure of the electrical submodel, for various fixed values of [ATP]. As for the Chay–Keizer model, we treat c as a slow variable and construct the bifurcation diagrams using c as a bifurcation parameter.

At all values of [ATP], the curve of steady states (labeled ss in Fig. 9.10) is Z-shaped. The unstable branches of this Z-shaped curve are shown as a dashed line. For low values of c the steady state becomes unstable in a Hopf bifurcation, from which emerges a branch of stable periodic solutions (the dot-dash curve, labeled $\text{osc}_{\max}$ and $\text{osc}_{\min}$ in Fig. 9.10, panel **a**).

As [ATP] increases, the Z-shaped curve moves to the right, but the $dc/dt = 0$ nullcline remains unchanged. Thus, when [ATP] is low, the $dc/dt = 0$ nullcline intersects the Z-shaped curve on the lower, stable, branch, a situation that gives no bursting at all (panel **a**). Conversely, when [ATP] is high, the $dc/dt = 0$ nullcline intersects the branch

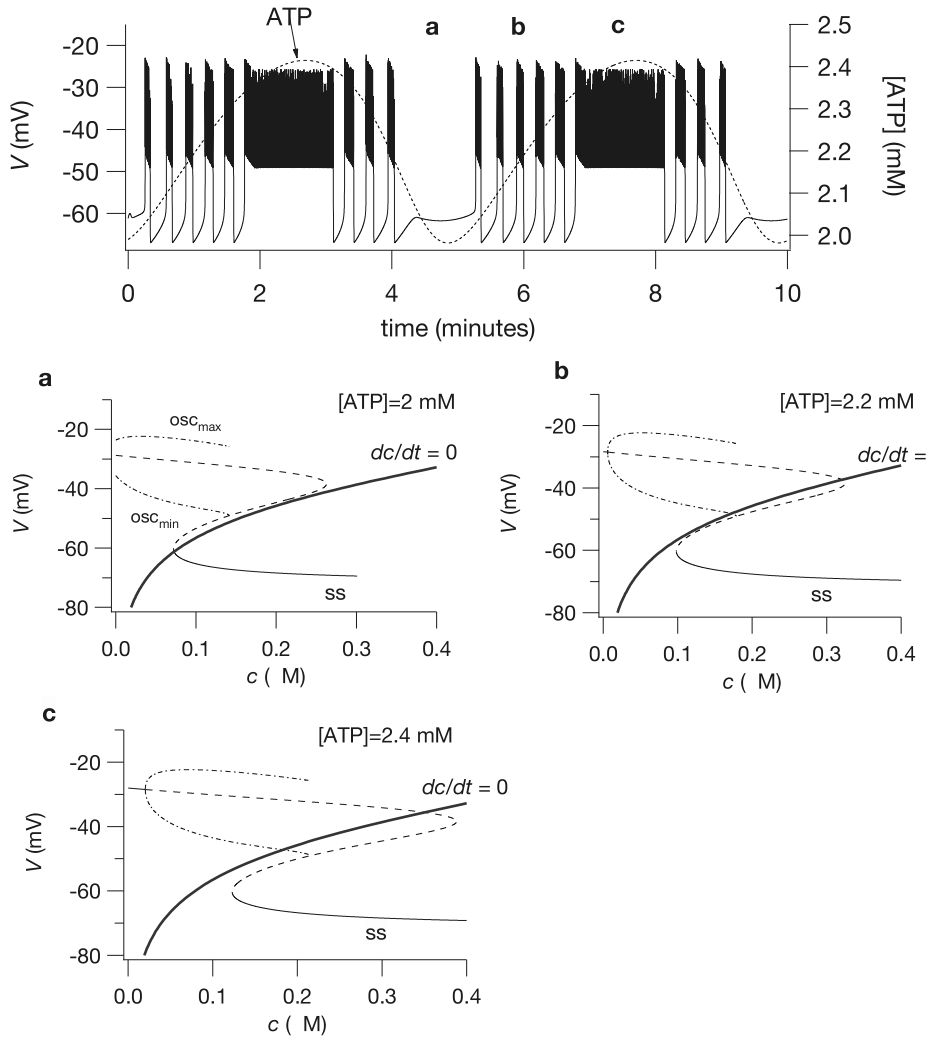

Figure 9.10 Compound bursting in the model with glycolytic oscillations. The upper panel shows a compound bursting pattern, in which the bursts are grouped in clusters that occur in a periodic manner. In panels **a**, **b**, and **c** are shown the bifurcation diagrams corresponding approximately to the regions labeled **a**, **b** and **c** in the top panel. The dashed lines are unstable branches of steady states, and the dot-dash lines are the maximum and minimum of stable periodic solutions.

of periodic orbits, which leads to a continuous active phase (panel **c**). When [ATP] takes intermediate values, the length of the active phase is either longer or shorter, depending on where the $dc/dt = 0$ nullcline intersects the Z-shaped curve (panel **b**).

Hence, as [ATP] varies over the course of an oscillation, so does the length of the active phase, thus giving compound bursting.